

AD-A086 967

WEAPONS SYSTEMS RESEARCH LAB ADELAIDE (AUSTRALIA)  
USE OF A NEW ANALYTICAL TECHNIQUE TO DETERMINE HEAT INPUT FROM --ETC(U)  
JAN 79 G JEPPI

F/G 20/4

UNCLASSIFIED

WSRL-0069-TR

NL

[ ]  
[ ]  
[ ]



END  
DATE  
FILMED  
9-80  
DTIC

WSRL-0069-TR

*B.S.*

AR-001-461



**LEVEL II**

**DEPARTMENT OF DEFENCE**

**DEFENCE SCIENCE AND TECHNOLOGY ORGANISATION**

**WEAPONS SYSTEMS RESEARCH LABORATORY**

DEFENCE RESEARCH CENTRE SALISBURY  
SOUTH AUSTRALIA

ADA 086967

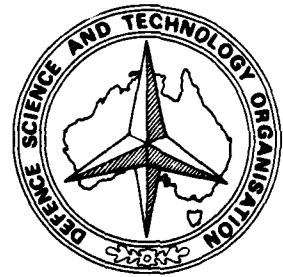
**TECHNICAL REPORT**

WSRL-0069-TR

**USE OF A NEW ANALYTICAL TECHNIQUE TO DETERMINE HEAT INPUT FROM  
INNER SURFACE TEMPERATURES MEASURED ON A HEMISPHERICAL SHELL  
DURING A FREE FLIGHT EXPERIMENT**

G. JEPPE

THE UNITED STATES NATIONAL  
TECHNICAL INFORMATION SERVICE  
IS AUTHORIZED TO  
REPRODUCE AND SELL THIS REPORT



Approved for Public Release

**DTIC ELECTE**  
**S D**  
JUL 23 1980

**D**

DDC FILE COPY

COPY No. 8

JANUARY 1979

80 7 22 008

Accession For	
NTIS GRA&I	
DOC TAB	
Unannounced Justification	
By _____	
Distribution/ _____	
Availability Codes	
Dist	Avail and/or special
<b>A</b>	

UNCLASSIFIED

DEPARTMENT OF DEFENCE

AR-001-461

DEFENCE SCIENCE AND TECHNOLOGY ORGANISATION

WEAPONS SYSTEMS RESEARCH LABORATORY

TECHNICAL REPORT

WSRL-0069-TR

USE OF A NEW ANALYTICAL TECHNIQUE TO DETERMINE HEAT INPUT FROM  
INNER SURFACE TEMPERATURES MEASURED ON A HEMISPHERICAL  
SHELL DURING A FREE FLIGHT EXPERIMENT

G. Jepps

S U M M A R Y

A free flight experiment has been conducted on a hemispherical shell to test a new technique for deriving outer surface temperature and heat transfer distributions from inner surface temperature measurements recorded from three arrays of thermocouples. The hemispherical shell which was mounted on the front of a rocket vehicle reached a maximum Mach number of 5.5 at 4 km altitude after 7 s of flight. Derived heat transfer profiles are characteristic of boundary layer flow which is laminar in the stagnation region, changing to turbulent within the first twenty degrees of arc. For the maximum heating profile, Stanton numbers varied between 0.0037 at 30° from the stagnation point and 0.0025 at 60°. The maximum free stream Reynolds number based on body diameter was  $26 \times 10^6$ . Agreement with laminar stagnation point heat transfer theory for steady flow is good except for just after maximum heating where the experimental results are some twenty five per cent higher. It is concluded that the new technique is successful but that the circumferential temperature and heat transfer resolutions could be improved by increasing the number of thermocouples in each array from seven to at least nine.

**S** DTIC  
ELECTE  
JUL 23 1980  
**D**

Approved for Public Release

POSTAL ADDRESS: Chief Superintendent, Weapons Systems Research Laboratory,  
Box 2151, G.P.O., Adelaide, South Australia, 5001.

UNCLASSIFIED

DOCUMENT CONTROL DATA SHEET

Security classification of this page

UNCLASSIFIED

<p>1 DOCUMENT NUMBERS</p> <p>AR Number: AR-001-461</p> <p>Report Number: WSRL-0069-TR ✓</p> <p>Other Numbers:</p>	<p>2 SECURITY CLASSIFICATION</p> <p>a. Complete Document: Unclassified</p> <p>b. Title in Isolation: Unclassified</p> <p>c. Summary in Isolation: Unclassified</p>
---	--

3 TITLE USE OF A NEW ANALYTICAL TECHNIQUE TO DETERMINE HEAT INPUT FROM INNER SURFACE TEMPERATURES MEASURED ON A HEMISPHERICAL SHELL DURING A FREE FLIGHT EXPERIMENT

<p>4 PERSONAL AUTHOR(S):</p> <p>G. Jepps</p>	<p>5 DOCUMENT DATE: 18.1.79</p>
<p>7.1 CORPORATE AUTHOR(S):</p> <p>Weapons Systems Research Laboratory ✓</p> <p>7.2 DOCUMENT SERIES AND NUMBER</p> <p>Weapons Systems Research Laboratory 0069-TR</p>	<p>6 6.1 TOTAL NUMBER OF PAGES 64</p> <p>6.2 NUMBER OF REFERENCES: 11</p>

<p>10 IMPRINT (Publishing organisation)</p> <p>Defence Research Centre Salisbury</p>	<p>8 REFERENCE NUMBERS</p> <p>a. Task: DST 76/118</p> <p>b. Sponsoring Agency:</p> <p>9 COST CODE: 137911</p>
--	---

<p>11 COMPUTER PROGRAM(S) (Title(s) and language(s))</p>
--

12 RELEASE LIMITATIONS (of the document):

Approved for Public Release

12.0	OVERSEAS	NO		P.R.	1	A		B		C		D		E
------	----------	----	--	------	---	---	--	---	--	---	--	---	--	---

Security classification of this page:

UNCLASSIFIED

## 13 ANNOUNCEMENT LIMITATIONS (of the information on these pages):

No limitation

## 14 DESCRIPTORS:

- |                        |  |  |
|------------------------|--|--|
| a. EJC Thesaurus Terms | Aerodynamic heating<br>Hemispherical shells<br>Stagnation point<br>Data processing | Aerothermodynamics<br>Aerodynamic heat transfer<br>Surface temperature<br>Free flight trajectories |
| b. Non-Thesaurus Terms | Stagnation point heating<br>Inverse heating<br>Free flight experiment              |  |

## 15 COSATI CODES:

2004

## 16 LIBRARY LOCATION CODES (for libraries listed in the distribution):

SW SR SD AACA

## 17 SUMMARY OR ABSTRACT:

(if this is security classified, the announcement of this report will be similarly classified)

A free flight experiment has been conducted on a hemispherical shell to test a new technique for deriving outer surface temperature and heat transfer distributions from inner surface temperature measurements recorded from three arrays of thermocouples. The hemispherical shell which was mounted on the front of a rocket vehicle reached a maximum Mach number of 5.5 at 4 km altitude after 7 s of flight. Derived heat transfer profiles are characteristic of boundary layer flow which is laminar in the stagnation region, changing to turbulent within the first twenty degrees of arc. For the maximum heating profile, Stanton numbers varied between 0.0037 at 30° from the stagnation point and 0.0025 at 60°. The maximum free stream Reynolds number based on body diameter was  $26 \times 10^6$ . Agreement with laminar stagnation point heat transfer theory for steady flow is good except for just after maximum heating where the experimental results are some twenty five per cent higher. It is concluded that the new technique is successful but that the circumferential temperature and heat transfer resolutions could be improved by increasing the number of thermocouples in each array from seven to at least nine.

## TABLE OF CONTENTS

	Page No.
1. INTRODUCTION	1
2. ROCKET TEST VEHICLE AND INSTRUMENTATION	2
3. THEORY AND METHOD	3
3.1 Derivation of Outer Surface Temperature	5
3.2 Derivation of Outer Surface Radial Heat Transfer	8
4. RESULTS AND DISCUSSION	11
5. CONCLUSIONS	14
6. ACKNOWLEDGEMENTS	14
NOTATION	15
REFERENCES	17

## LIST OF FIGURES

1. Photograph of rocket test vehicle on launcher
2. Sketch of rocket test vehicle
3. Flight path showing recovery events
4. Mach number, free stream Reynolds number, altitude, and stagnation temperature histories
5. Photograph of hemisphere and instrumentation compartment just after impact
6. Positions of thermocouples and differential pressure yawmeter holes
7. Raw temperature measurements (stagnation point  $\theta=0$ )
8. Raw temperature measurements ( $\phi=0$ ,  $\theta=20^\circ$ ,  $30^\circ$ ,  $40^\circ$ )
9. Raw temperature measurements ( $\phi=120^\circ$ ,  $\theta=20^\circ$ ,  $30^\circ$ ,  $40^\circ$ )
10. Raw temperature measurements ( $\phi= -120^\circ$ ,  $\theta=20^\circ$ ,  $30^\circ$ ,  $40^\circ$ )
11. Raw temperature measurements (superpositioning of  $\phi=0$  upon  $\phi=120^\circ$  for  $\theta=20^\circ$ ,  $30^\circ$ ,  $40^\circ$ )
12. Raw temperature measurements ( $\phi=0$ ,  $\theta=50^\circ$ ,  $70^\circ$ ,  $90^\circ$ )
13. Raw temperature measurements ( $\phi=120^\circ$ ,  $\theta=50^\circ$ ,  $70^\circ$ ,  $90^\circ$ )
14. Raw temperature measurements ( $\phi= -120^\circ$ ,  $\theta=50^\circ$ ,  $70^\circ$ ,  $90^\circ$ )
15. Coordinate system for hemispherical shell

16. Amplitude and frequency of the Fourier components of temperature ( $\phi=120^\circ$ ,  $\theta=20^\circ$ )
17. Amplitude and frequency of the Fourier components of temperature ( $\phi=120^\circ$ ,  $\theta=30^\circ$ )
18. Amplitude and frequency of the Fourier components of temperature ( $\phi=120^\circ$ ,  $\theta=40^\circ$ )
19. Fourier smoothed and seven-component Legendre temperature representation superimposed on raw data ( $\phi=120^\circ$ ,  $\theta=20^\circ$ ,  $30^\circ$ ,  $40^\circ$ )
20. Fourier smoothed and seven-component Legendre temperature representation superimposed on raw data ( $\phi=0$ ,  $\theta=50^\circ$ ,  $70^\circ$ ,  $90^\circ$ )
21. Derived outer surface temperature distribution ( $\phi=0$ )
22. Derived outer surface temperature distribution ( $\phi=120^\circ$ )
23. Derived outer surface temperature distribution ( $\phi= -120^\circ$ )
24. Derived outer surface heat transfer distribution ( $\phi=0$ ,  $t \leq 6s$ )
25. Derived outer surface heat transfer distribution ( $\phi=120^\circ$ ,  $t \leq 6s$ )
26. Derived outer surface heat transfer distribution ( $\phi= -120^\circ$ ,  $t \leq 6s$ )
27. Derived outer surface heat transfer distribution ( $\phi=0$ ,  $t \geq 6.4s$ )
28. Derived outer surface heat transfer distribution ( $\phi=120^\circ$ ,  $t \geq 6.4s$ )
29. Derived outer surface heat transfer distribution ( $\phi= -120^\circ$ ,  $t \geq 6.4s$ )
30. Outer surface heat transfer and inner surface temperature time derivative for  $\theta=20^\circ$
31. Scatter of derived outer surface heat transfer at stagnation point,  $\theta=0$
32. Stanton number distribution ( $\phi=0$ ,  $t \leq 6s$ )
33. Stanton number distribution ( $\phi=120^\circ$ ,  $t \leq 6s$ )
34. Stanton number distribution ( $\phi= -120^\circ$ ,  $t \leq 6s$ )
35. Stanton number distribution ( $\phi=0$ ,  $t \geq 6.4s$ )
36. Stanton number distribution ( $\phi=120^\circ$ ,  $t \geq 6.4s$ )
37. Stanton number distribution ( $\phi= -120^\circ$ ,  $t \geq 6.4s$ )
38. Comparison of derived stagnation point Stanton number with laminar theory
39. Comparison of derived stagnation point heat transfer with laminar theory
40. Peak turbulent heating envelope

## 1. INTRODUCTION

This report describes the results of a free flight rocket experiment which, although conducted in 1971, has nevertheless not been formally recorded until now. This experiment marked the end of a long program of collaboration between the Royal Aircraft Establishment, UK, and Weapons Research Establishment. Under this collaborative program a hypersonic research rocket was developed and a series of these rocket vehicles was used to conduct experiments aimed primarily at investigating heat transfer and pressure distribution on wings and noses of various shapes. In the experiment described in this report a new technique has been used to deduce the heat transfer to the outer surface of a hemispherical shell-shaped nose in flight from measurements of its inner surface temperature. Of particular interest was the peak turbulent heating and the stagnation point heating. This shell was 282 mm in diameter, 3.18 mm thick, and made from Inconel steel.

To deduce heated surface conditions from inner temperature measurements is not altogether straightforward and the problem is a member of the class known as inverse problems, where the quantity to be deduced cannot be expressed explicitly in terms of the measured quantity. The greater the thickness of the shell, the greater the difficulty becomes, until a solution eventually becomes impossible. However, during other work carried out within the Weapons Research Establishment on designing and analysing heat transfer experiments some techniques have been discovered which delay the onset of these difficulties enabling thicker shells to be used. These techniques have been put to use in the present experiment where the Inconel steel hemispherical shell was thin enough to make an inverse problem solution feasible under conditions of high turbulent heat transfer, but thick enough to escape melting when boosted to Mach 5.5 at altitude 3.7 km in 6.8 s.

More light on the nature of the difficulty with the inverse heating problem as such can be shed by considering one-dimensional heat flow across a wall heated on one surface and insulated at the other. Here, using the Fourier heat conduction equation as the mathematical model, leads to an integral equation which relates the insulated surface temperature explicitly to an integral containing the heated surface temperature. This integral equation cannot be inverted analytically to give the heated surface temperature explicitly in terms of the insulated surface temperature which would be the measured quantity in the present problem. When the heated surface temperature variation is approximated by a tabulated function with values given at regular time intervals of  $\delta$ , the integral equation reduces to algebraic recurrence relationships which can be inverted to give heated surface heat flow and temperature in tabular form expressed explicitly in terms of tabulated insulated surface measurements and previously calculated heated surface temperatures. One might now think that this approximate solution can be taken to the accuracy required by making the time step  $\delta$  small enough. This turns out not to be the case. The effect of making  $\delta$  smaller is to introduce higher frequency terms in representing the inaccuracies of the algebraic process and insulated surface temperatures magnify in proportion to their frequencies when translated into heated surface temperatures. This magnification is dependent not only on the time step  $\delta$  but also on the ability of the wall to diffuse heat, the diffusivity  $\alpha$ , and the wall thickness  $l$ . The relevant nondimensional frequency parameter for tabulated data is  $\alpha \delta / l^2$  and below a certain critical value of this parameter the algebraic inversion process can become violently unstable. On the other hand, if the time step  $\delta$  has to be made too large to avoid this instability, the data will lose its sharpness and features of the temperature profiles will be lost. Fortunately there is a way around this problem which allows the time step  $\delta$  to be chosen so that the temperature profile features are retained and the onset of numerical instability is delayed. This is brought about by what is termed the wall-splitting technique which uses the fact that for one-dimensional heat flow a wall can be treated exactly as an equivalent number of walls of lesser thickness. This then has the effect of reducing the thickness  $l$  for each sub-wall, thus increasing the

parameter a  $\delta/l^2$  without increasing  $\delta$ . Although this seems to have the disadvantage that a number of walls have to be treated instead of just one, the accumulative error incurred by repeated stable algebraic inversion processes does remain small. The foregoing discussion relates to one-dimensional heat flow and the next question is how to relate this to the assumed two-dimensional heat flow in the hemispherical shell.

The hemispherical shell is assumed to be heated axisymmetrically about the longitudinal axis of symmetry normal to its base. Thus the mathematical model of the heat conduction is the two-dimensional Fourier heat conduction equation in spherical polar coordinates where heat flows radially and circumferentially in meridian planes containing the longitudinal axis of symmetry. The components of temperature arising from the circumferential heat flow are separated out by an expansion of the temperature solution into an infinite series of Legendre polynomials whose coefficients are functions of time and radial position. These coefficients satisfy an equation somewhat similar to the equation satisfied by temperature in one-dimensional heat flow across plane walls. Thus a somewhat modified form of the wall-splitting technique for plane walls can be adapted to these coefficients for application to hemispherical shells.

So far the question of noise on the experimental temperature measurements has not been mentioned. Because the derivation of heated surface temperature from insulated surface temperature is essentially a magnification process the presence of noise on the insulated surface measurements is very troublesome and raw data must be smoothed before being used in the heated surface temperature derivation process. The temperature profiles measured in this experiment are very well defined, there being about 10 s of record for each thermocouple sampled at 80 points/s. This type of data is particularly suited to overall smoothing by Fourier analysis, using sine series. A linear temperature variation with time is combined with the temperature record to be smoothed, the two constants being chosen such that the value of the combined function is zero at each end. When this combined function is regarded as an odd function of time, both it and its first derivative are continuous at the end points with the consequence that the resulting Fourier sine series expansion tends to converge as  $n^{-3}$  where  $n$  is the term number. At least this is true for the smooth part of the function but, when the noise begins to dominate in the higher frequency components, this tendency to converge disappears and the higher order terms assume random amplitudes within the band of noise level. This distinctive behaviour enables noise to be separated from the smooth part of the function in Fourier smoothing. In this experiment, with about 800 points per record there is enough redundant information to be able to least-squares fit a 300 term Fourier sine series to each record. Another advantage of Fourier smoothing in free flight experiments is that it enables spurious frequencies to be detected such as those which may arise from rotary switches or structural vibrations.

The object of this experiment is to provide a practical test for the techniques previously mentioned and at the same time to acquire some meaningful information on the surface heat flux and temperature distributions around a hemispherical nose during low altitude supersonic flight. In the next section a description of the rocket test vehicle, its performance and instrumentation, is given. A fuller account of the theory and method together with references is given in Section 3 and a discussion of the results and an assessment of the techniques used is given in Section 4.

## 2. ROCKET TEST VEHICLE AND INSTRUMENTATION

The hemispherical shell tested formed the nose of the rocket vehicle shown in figures 1 and 2. Further details of this rocket vehicle together with reasons for using it are given in reference 1. Trajectory data were obtained from radio Doppler, Contraves kinetheodolites, and radar. Vinten cameras were also used to monitor the

behaviour of the vehicle itself during flight. The vehicle performed satisfactorily and at apogee the hemisphere attached to the instrumentation compartment was separated from the boost motor to be recovered intact on the ground some 21 km downrange after deploying first a drogue and then a parachute. The sequence of events leading to recovery is shown in figure 3. Figure 4 shows Mach number, free stream Reynolds number, altitude, and stagnation temperature histories for the first nine seconds of flight. Figure 5 shows a photograph, taken shortly after impact on the Woomera range, of the hemisphere and instrumentation compartment with the recovery parachute still attached. No discernible damage was suffered by the hemisphere which with thermocouples intact is available for further experiment, either wind tunnel or flight.

The diameter of the hemispherical shell was 282 mm, its thickness was 3.18 mm and it was made out of 'Inconel 600,' a material chosen because its thermal diffusivity varied less with temperature than other available materials and the mathematical model used for the heating analysis was based on constant diffusivity. To ensure the presence of fully turbulent flow on at least part of the hemisphere the outer surface was finished to a roughness, nowhere less than  $0.64 \mu\text{m}$ . Nineteen chromel-alumel thermocouples were spot welded to the inner surface of the shell along three generators in planes 120 degrees apart, their positions being shown in figure 6 together with four pressure monitoring holes connected to a differential pressure yawmeter. To reduce heat conduction losses, a durestos insulating ring one inch thick was inserted between the base of the hemisphere and the instrumentation compartment and a hemispherical radiation reflecting surface was fitted within the shell. Again, the mathematical model of heat conduction in the shell assumed that no heat crossed the inner surface or the base.

The instrumentation compartment carried a 24 channel 465 MHz telemetry system which transmitted data to ground receivers. Nineteen channels were used to transmit temperature data from each thermocouple at the rate of eighty points per second, one channel was used for the synchronising pulses needed to identify data on records, another for inductance calibrations, and the remaining three were sub-commutated so that each could sample twenty four different inputs. One of the sub-commutated channels carried data from all the inductance transducers used to measure lateral and longitudinal acceleration and yaw meter differential pressures. The other two sub-commutated channels carried data from two sun cells, from the recovery system monitor, and voltage calibrations including inputs from a cold junction and ten thermistors for subsequent calibration of thermocouple output. Telemetered data after being received on the ground was recorded in analogue form on magnetic tape and subsequently converted to digital form for input to a computer program which used the in-flight calibrations to produce time histories of the physical quantities being measured.

No rolling motion was evident during the first nine-seconds of flight from either the sun cell records or from the Vinten camera film. Incidence history as deduced from the differential pressure yawmeter was obviously wrong; the results showed an incidence of half a degree for the first five seconds followed by a steady increase of about one degree per second which would have led to break up of the vehicle's structure. The raw temperature measurements from each of the nineteen thermocouples are shown in figures 7 to 14 covering the first nine seconds of flight.

### 3. THEORY AND METHOD

The mathematical model of the heat conduction used in this analysis is that of a hemispherical shell of inner radius  $a$  and outer radius  $b$ , having constant thermal diffusivity  $\alpha$ . The symmetry of the external heating is assumed to be such that heat can flow only in the  $r$  and  $\theta$  directions shown in figure 15; then the temperature at a point  $\mu$ ,  $r$ , at time  $t$ ,  $T(\mu, r, t)$ , where  $\mu = \cos \theta$ , is given by the equation

$$\frac{1}{r^2} \left[ \frac{\partial}{\partial r} \left( r^2 \frac{\partial T}{\partial r} \right) + \frac{\partial}{\partial \mu} \left\{ (1 - \mu^2) \frac{\partial T}{\partial \mu} \right\} \right] = \frac{1}{a} \frac{\partial T}{\partial t} \quad (1)$$

Details of the derivation of this equation can be found in reference 2. It is well known that solutions of this equation can be expanded in series of Legendre polynomials in  $\mu$  where the coefficients are functions of  $r$  and  $t$ . A convenient way of arriving at this result for the purpose of the present analysis is to introduce the integral transform

$$\tilde{T}_{2n}(r,t) = \int_0^1 T(\mu, r, t) P_{2n}(\mu) d\mu \quad (2)$$

In equation (2) the  $P_{2n}(\mu)$  are Legendre polynomials of order  $2n$  in even powers of  $\mu$  and the  $\tilde{T}_{2n}(r,t)$  can be considered as Legendre components of temperature  $T(\mu, r, t)$ . In fact temperatures are reconstituted from their Legendre components by the inverse transformation

$$T(\mu, r, t) = \sum_{n=0}^{\infty} (4n+1) P_{2n}(\mu) \tilde{T}_{2n}(r, t) \quad (3)$$

To find the  $\tilde{T}_{2n}(r,t)$ , the integral transform given by equation (2), when applied to equation (1) gives

$$\frac{1}{r^2} \frac{\partial}{\partial r} \left\{ r^2 \frac{\partial \tilde{T}_{2n}}{\partial r} \right\} - \frac{2n(2n+1)}{r^2} \tilde{T}_{2n} = \frac{1}{a} \frac{\partial \tilde{T}_{2n}}{\partial t} \quad (4)$$

where it has been assumed that no heat passes through the plane  $\theta = \frac{\pi}{2}$ , which implies the condition  $\frac{\partial T}{\partial \mu} = 0$  at  $\mu = 0$ . To provide for this condition in the experiment a durestos ring was used to insulate the base of the hemisphere from the adjoining instrumentation compartment. It should be noted here too, that  $T$  in equations (2) and (3) can be replaced by the radial heat flow  $Q_r$  which is given by  $-K \frac{\partial T}{\partial r}(\mu, r, t)$  with Legendre component  $\tilde{Q}_{2n}(r, t)$  defined by  $-K \frac{\partial \tilde{T}_{2n}}{\partial r}(r, t)$ , where  $K$  is the coefficient of thermal conductivity for the shell material.

In this experiment, temperature histories were measured by three rows of thermocouples attached to the inner surface  $r=a$  of the hemisphere and are shown in figures 7 to 14. Hence in order to use a one-dimensional analysis based on equation (4) to deduce temperature and radial heat flow at the outer surface  $r=b$ , it is necessary to first find the Legendre components  $\tilde{T}_{2n}(a, t)$  of the measured temperatures. This was accomplished by fitting piecewise quadratics in  $\mu$  to the time-smoothed measurements  $T(\mu, a, t)$  through each three successive  $\mu$  positions along each row of thermocouples. These quadratic expressions for  $T(\mu, a, t)$  were then inserted into equation (2) from which values of  $\tilde{T}_{2n}(a, t)$  up to  $n=6$  were calculated. Thus only a truncated version of equation (3) was used in reconstituting temperatures and heat flows from their Legendre components.

The method used for deriving  $\tilde{T}_{2n}(b, t)$  and  $\tilde{Q}_{2n}(b, t)$  from equation (4) follows

similar lines to that used for deriving outer surface temperature and heat flow from inner surface temperature history measurements taken on flat plates. The solution of equation (4) when no heat passes across the surface  $r=a$  can be extracted from reference (2) or obtained directly from reference (4), and is

$$\begin{aligned} \tilde{T}_{2n}(r,t) = & \left(\frac{b}{r}\right)^{\frac{1}{2}} \left[ \frac{\left(\frac{a}{r}\right)^{2n+\frac{1}{2}} + \left(\frac{r}{a}\right)^{2n+\frac{1}{2}} \left(1 + \frac{1}{2n}\right)}{\left(\frac{a}{b}\right)^{2n+\frac{1}{2}} + \left(\frac{b}{a}\right)^{2n+\frac{1}{2}} \left(1 + \frac{1}{2n}\right)} \right] \tilde{T}_{2n}(b,t) \\ & + \left(\frac{b}{r}\right)^{\frac{1}{2}} \left[ \int_{S=0}^{\infty} \frac{B_{2n+\frac{1}{2}}(\sigma_s, r)}{\frac{1}{2} \sigma_s \frac{\partial}{\partial \sigma_s} B_{2n+\frac{1}{2}}(\sigma_s, b)} \int_0^t \frac{\partial \tilde{T}_{2n}(b, \xi)}{\partial \xi} e^{-\sigma_s^2 a(t-\xi)} d\xi \right], \end{aligned} \quad (5)$$

where

$$\begin{aligned} B_{2n+\frac{1}{2}}(\sigma_s, r) = & J_{2n+\frac{1}{2}}(\sigma_s r) \left\{ \frac{1}{2} Y_{2n+\frac{1}{2}}(\sigma_s a) - \sigma_s a Y'_{2n+\frac{1}{2}}(\sigma_s a) \right\} \\ & - Y_{2n+\frac{1}{2}}(\sigma_s r) \left\{ \frac{1}{2} J_{2n+\frac{1}{2}}(\sigma_s a) - \sigma_s a J'_{2n+\frac{1}{2}}(\sigma_s a) \right\}, \end{aligned} \quad (6)$$

$J_{2n+\frac{1}{2}}$  and  $Y_{2n+\frac{1}{2}}$  are Spherical Bessel Functions of the first and second kinds respectively and  $\sigma_s$  is the  $s$ th zero of  $B_{2n+\frac{1}{2}}(\sigma, b)$ . The properties of Spherical Bessel Functions are given in reference 3 where they are shown to be expressible in the form

$$\begin{aligned} J_{2n+\frac{1}{2}}(Z) &= \sqrt{\frac{2Z}{\pi}} \left\{ f_{2n}(Z) \sin Z - f_{-2n-1}(Z) \cos Z \right\} \\ Y_{2n+\frac{1}{2}}(Z) &= -\sqrt{\frac{2Z}{\pi}} \left\{ f_{2n}(Z) \cos Z + f_{-2n-1}(Z) \sin Z \right\} \end{aligned}$$

and the  $f_m(Z)$  are finite polynomials in negative powers of  $Z$  such that

$$\begin{aligned} f_{m-1}(Z) + f_{m+1}(Z) &= (2m+1) Z^{-1} f_m(Z), \quad (m=0, \pm 1, \pm 2, \dots) \\ f_0(Z) &= Z^{-1} \quad \text{and} \quad f_1(Z) = Z^{-2} \end{aligned}$$

Thus the Spherical Bessel Functions for the hemispherical shell are simply related to the circular functions  $\cos Z$ ,  $\sin Z$ , which occur without the  $f_m$  polynomials in one-dimensional flat plate heat conduction theory. In fact, equation (5) is similar in form to the flat plate solution which links the inner insulated surface temperature with the outer heated surface temperature.

### 3.1 Derivation of Outer Surface Temperature

The difficulties in deriving  $\tilde{T}_{2n}(b,t)$  from  $\tilde{T}_{2n}(a,t)$  through equation (5) with  $r=a$ , are similar in nature to the flat plate inverse problem, so that the devices used to conquer that problem can also be applied to the shell.

Because there is no explicit way in which  $\tilde{T}(b,t)$  can be expressed as a continuous analytic function of  $\tilde{T}(a,t)$ , a finite difference approach is adopted in determining  $\tilde{T}(b,t)$  from  $\tilde{T}(a,t)$  through equation (5) with  $r=a$ . This method is explained in detail in reference (4). In short,  $\tilde{T}_{2n}(b,t)$  is considered to consist of a series of chords joining the points  $\tilde{T}_{2n}(b, \overline{r-1} \delta)$  to  $\tilde{T}_{2n}(b, r \delta)$ , where  $r$  ranges in integer values from 1 to  $m$  and  $m \delta = t$ . Substituting these values for  $\tilde{T}_{2n}(b,t)$  into equation (5) gives the following result for the Legendre components of the shell inner insulated surface temperature

$$\tilde{T}_{2n}(a,t) = \left(\frac{b}{a}\right)^{\frac{1}{2}} \left[ \frac{(4n+1) \left(\frac{b}{a}\right)^{2n+1}}{2n+ (2n+1) \left(\frac{b}{a}\right)^{4n+1}} \right]$$

$$+ \left(\frac{b}{a}\right)^{\frac{1}{2}} \left[ \int_{s=0}^{\infty} \frac{B_{2n+\frac{1}{2}}(\sigma_s, a)}{\sigma_s^{\frac{1}{2}} \frac{\partial}{\partial \sigma_s} B_{2n+\frac{1}{2}}(\sigma_s, b)} \sum_{r=1}^m \frac{1}{\delta} \int_{\frac{r-1}{r-1} \delta}^{r \delta} \left\{ \tilde{T}_{2n}(b, r \delta) - \tilde{T}_{2n}(b, \overline{r-1} \delta) \right\} e^{-\sigma_s^2 a (m \delta - \xi)} d \xi \right]$$

which, on evaluating the integral, can be written in the form

$$\tilde{T}_{2n}(b, m \delta) = \frac{1}{\Theta_{1,n}} \left[ \tilde{T}_{2n}(a, m \delta) - \sum_{r=1}^{m-1} \tilde{T}_{2n}(b, r \delta) \Theta_{m-r+1,n} \right], \quad (7)$$

where

$$\Theta_{1,n} = \frac{(4n+1) \left(\frac{b}{a}\right)^{2n+1}}{2n+ (2n+1) \left(\frac{b}{a}\right)^{4n+1}} - \frac{4}{\pi a \delta} \left(\frac{b}{a}\right)^{\frac{1}{2}} \int_{s=0}^{\infty} \frac{(1 - e^{-\sigma_s^2 a \delta})}{\sigma_s^3 \frac{\partial}{\partial \sigma_s} B_{2n+\frac{1}{2}}(\sigma_s, b)}, \quad (8)$$

$$\Theta_{m-r+1,n} = \frac{4}{\pi a \delta} \left(\frac{b}{a}\right)^{\frac{1}{2}} \int_{s=0}^{\infty} \frac{(1 - e^{-\sigma_s^2 a \delta^2}) e^{-\sigma_s^2 a \delta (m-r-1)}}{\sigma_s^3 \frac{\partial}{\partial \sigma_s} B_{2n+\frac{1}{2}}(\sigma_s, b)} \quad (9)$$

and the  $\sigma_s$  are the zeros of equation (6) with  $r=b$ .

Thus equations (7), (8) and (9), allow  $\tilde{T}_{2n}(b, m \delta)$  to be calculated from a series of algebraic recurrence relationships involving  $\tilde{T}_{2n}(a, m \delta)$  and the previously calculated values of  $\tilde{T}_{2n}(b, r \delta)$ .

However, the calculation of an outer heated surface temperature from a known inner insulated surface is essentially a magnification process. Thus any noise on experimental data or errors inherent in numerical procedures tend to become magnified. It is shown in reference (2) that the amplitude magnification is greater on the higher frequency components of the inner insulated surface temperature. In this experiment the higher frequency components stem from noise in the measured temperatures and from the step size  $\delta$  used in the numerical calculation procedure. To a large extent the high frequency noise in the temperature measurements has been removed by a Fourier smoothing process which fits a Fourier sine series about a straight line to represent each temperature-time record and truncates the series at some pre-assigned cut-off frequency. Under these conditions the Fourier representation of a continuous signal tends to converge as  $n^{-3}$  whereas a discontinuous noise component has no tendency to converge. This effect is well illustrated in figures 16, 17 and 18, which show the relationship between amplitude and frequency for the temperature measurements taken at  $\phi = 120^\circ$ ,  $\theta = 20^\circ$ ,  $30^\circ$ , and  $40^\circ$ . In these figures, the amplitude noise band has been chosen to include amplitude values which obviously exhibit random behaviour. Starting with the lower frequencies, the standard deviation of these random amplitudes approaches a limit as the number of values included is increased. A cut-off amplitude corresponding to a fixed multiple of this limiting value of the standard deviation of the random amplitudes is then selected and only amplitudes above this cut-off value are retained to represent smoothed temperatures. For this experiment, only amplitudes greater than six standard deviations of the random amplitudes have been retained. The smoothed temperature was represented by a straight line plus the first four Fourier terms for  $\theta = 20^\circ$ , whereas the first six terms were used in representing  $\theta = 30^\circ$  and  $\theta = 40^\circ$ . These smoothed temperature representations are shown superimposed on the raw data in figure 19. Smoothed temperatures for  $\phi = 0$ ,  $\theta = 50^\circ$ ,  $70^\circ$  and  $90^\circ$  are shown in figure 20 where six Fourier terms were used for  $\theta = 50^\circ$  and four for each of  $\theta = 70^\circ$  and  $\theta = 90^\circ$ . Having removed the high frequency noise from the raw data the Legendre components of the smoothed temperatures are represented as tabulated functions with values given at regular time intervals  $\delta$ . These values, when introduced into equation (7), which is the algebraic inversion process for calculating the outer surface temperature components  $\tilde{T}_{2n}(b, m \delta)$ , have the effect of introducing an error of frequency  $\delta$ . The larger the thermal thickness of the shell and the smaller the time step  $\delta$  the greater the amplification of this error in the derived temperature components. This behaviour is just contrary to what is required; the shell needs to be thermally thick enough to survive the high turbulent low-altitude heating while the larger the time step  $\delta$  the coarser the numerical temperature representation. This problem can be eased by splitting the shell thickness into a number of smaller thicknesses for the purpose of calculation. The way in which this works is best illustrated by briefly describing the wall splitting technique as given in reference 5 for flat plates. Applying the

operational transform  $\tilde{T}(x, p) = p \int_0^\infty T(x, t) e^{-pt} dt$  to the one-dimensional

heat conduction equation  $\frac{\partial^2 T(x, t)}{\partial x^2} = \frac{1}{a} \frac{\partial T(x, t)}{\partial t}$  gives the solution

$$\tilde{T}(l, p) = \frac{\tilde{T}(0, p)}{\cosh \sqrt{\frac{p}{a}} l} \quad (10)$$

when heat is received at the surface  $x=0$  and no heat passes across  $x=1$ . Equation (10) can be re-written as

$$\tilde{T}(0,p) = \tilde{T}(1,p) \operatorname{Cosh} \sqrt{\frac{p}{a}} 1$$

where  $\operatorname{Cosh} \sqrt{\frac{p}{a}} 1$  can be regarded as the operator which when applied to the transform of the insulated surface temperature gives the transform of the heated surface temperature. Now  $\operatorname{Cosh} \sqrt{\frac{p}{a}} 1$  can be expanded in terms of multiple arguments to generate operators representing walls of thickness less than 1. The simplest expansion of this type is to put  $\operatorname{Cosh} \sqrt{\frac{p}{a}} 1 = 2 \operatorname{Cosh}^2 \sqrt{\frac{p}{a}} \frac{1}{2} - 1$ , which when substituted into equation (10) gives

$$\tilde{T}(0,p) = 2 \tilde{T}(1,p) \operatorname{Cosh}^2 \sqrt{\frac{p}{a}} \frac{1}{2} - \tilde{T}(1,p)$$

This result is interpreted to mean that the temperature  $T(1,t)$  is applied to the insulated surface of a wall of half the original thickness and the outer surface temperature so obtained is then itself applied to the insulated surface of the same half-thickness wall. The outer surface temperature obtained from this second operation is then doubled and the original  $T(1,t)$  subtracted to give the outer surface temperature sought after. Because, as previously mentioned, the Spherical Bessel Functions of the solutions to heat conduction in a hemisphere are simply related to the circular functions of the flat plate solutions, the wall-splitting technique can be applied to a hemispherical shell and this is shown in reference 6. In fact, the computer program described in reference 6 for calculating shell outer surface temperatures from inner surface temperatures, as used in this experiment, allows the shell thickness to be subdivided up to six times.

When the error amplification effects become large, the numerical calculation of outer surface temperature by a process such as equation (7) can suddenly become violently unstable causing the calculated results to oscillate wildly. This feature renders the onset of instability very easy to detect in running a computer program, so that a method of automatically introducing a wall-splitting is readily arranged. The tendency to amplify errors manifests itself through

$\Theta_{1,n}$  in equation (7) where it is found that  $\Theta_{1,n}$  decreases as  $\frac{a\delta}{(b-a)^2}$  decreases.

It is of interest to note that both Pope and Heron, in references (7) and (8), found independently, that to avoid instability in this method of calculating outer heated surface temperature from inner insulated surface temperature for flat plates of thickness 1,  $\frac{a\delta}{l^2}$  must be greater than 2/3.

### 3.2 Derivation of Outer Surface Radial Heat Transfer

The Legendre components of the outer surface heat transfer are determined from the outer surface temperature components as calculated by equation (7). This is achieved by putting

$$\tilde{Q}_{2n}(b,t) = -k \left. \frac{\partial \tilde{T}}{\partial r}(r,t) \right|_{r=b}$$

which, from equation (5), gives

$$\begin{aligned} \frac{\tilde{Q}_{2n}(b,t)}{K} &= \frac{2n(2n+1)}{b} \left\{ \frac{\left(\frac{b}{a}\right)^{4n+1} - 1}{(2n+1)\left(\frac{b}{a}\right)^{4n+1} + 2n} \right\} \tilde{T}_{2n}(b,t) \\ &+ \sum_{s=0}^{\infty} \left[ \frac{\frac{\partial}{\partial r} B_{2n+\frac{1}{2}}(\sigma_s, r)}{\frac{1}{2} \sigma_s \frac{\partial}{\partial \sigma_s} B_{2n+\frac{1}{2}}(\sigma_s, b)} \right]_{r=b} \int_0^t \frac{\partial \tilde{T}_{2n}(b, \xi)}{\partial \xi} e^{-\sigma_s^2 a(t-\xi)} d\xi \end{aligned} \quad (11)$$

Although it is not apparent from this form of the solution, an alternative solution suitable for small values of time shows that the coefficient of  $\frac{\partial \tilde{T}_{2n}}{\partial \xi}$  in equation (11) behaves as  $C(t-\xi)^{-\frac{1}{2}}$  as  $\xi \rightarrow t$ , where  $C$  is a constant. Thus to employ the approximation that  $\frac{\partial \tilde{T}_{2n}(b, \xi)}{\partial \xi}$  can be taken as  $\frac{1}{\delta} \left\{ \tilde{T}_{2n}(b, r\delta) - \tilde{T}_{2n}(b, \overline{r-1}\delta) \right\}$  for  $\overline{r-1}\delta < \xi < r\delta$

in equation (11), it is advisable to integrate out the singularity that occurs as  $\xi \rightarrow t$ . This is achieved by integrating both sides of equation (11) from  $t-\delta$  to  $t$ , giving

$$\int_{t-\delta}^t \frac{\tilde{Q}_{2n}(b, \xi)}{K} d\xi = \frac{2n(2n+1)}{b} \left\{ \frac{\left(\frac{b}{a}\right)^{4n+1} - 1}{(2n+1)\left(\frac{b}{a}\right)^{4n+1} + 2n} \right\} \int_{t-\delta}^t \tilde{T}_{2n}(b, \xi) d\xi \quad (12)$$

$$+ \sum_{s=0}^{\infty} \left[ \frac{\frac{\partial}{\partial r} B_{2n+\frac{1}{2}}(\sigma_s, r)}{\frac{1}{2} \sigma_s \frac{\partial}{\partial \sigma_s} B_{2n+\frac{1}{2}}(\sigma_s, b)} \right]_{r=b} \int_{t-\delta}^t \int_0^{\xi} \frac{\partial \tilde{T}_{2n}(b, \xi_1)}{\partial \xi_1} e^{-\sigma_s^2 a(\xi-\xi_1)} d\xi_1 d\xi$$

After changing the order of integration in the double integral, one integration can be performed and when  $\frac{\partial \tilde{T}_{2n}(b, \xi_1)}{\partial \xi_1}$  is replaced by

$$\frac{1}{\delta} \left\{ \tilde{T}_{2n}(b, r\delta) - \tilde{T}_{2n}(b, \overline{r-1}\delta) \right\} \text{ for } \overline{r-1}\delta < \xi < r\delta \text{ and } \int_{t-\delta}^t \tilde{Q}_{2n}(b, \xi) d\xi \text{ and}$$

$$\int_{t-\delta}^t \tilde{T}_{2n}(b, \xi) d\xi \text{ are approximated by } \frac{\delta}{2} \left\{ \tilde{Q}_{2n}(b, t) + \tilde{Q}_{2n}(b, t-\delta) \right\} \text{ and}$$

$\frac{\delta}{2} \left\{ \tilde{T}_{2n}(b, t) + \tilde{T}_{2n}(b, t - \delta) \right\}$  respectively, equation (12) becomes

$$\tilde{Q}_{2n}(b, m \delta) = \tilde{Q}_{2n}(b, \overline{m-1} \delta) + \tilde{T}_{2n}(b, m \delta) M_{1,n} + \tilde{T}_{2n}(b, \overline{m-1} \delta) M_{2,n} \quad (13)$$

$$+ \sum_{r=1}^{m-2} \tilde{T}_{2n}(b, r \delta) M_{m-r+1, n},$$

where

$$M_{1,n} = \frac{4K}{a^2 \delta^2} \sum_{s=0}^{\infty} \frac{\left[ \frac{\partial}{\partial r} B_{2n+\frac{1}{2}}(\sigma_s, r) \right]_{r=b}}{\sigma_s^5 \frac{\partial}{\partial \sigma_s} B_{2n+\frac{1}{2}}(\sigma_s, b)} \left\{ e^{-\sigma_s^2 a \delta} - 1 + \sigma_s^2 a \delta \right\} \quad (14)$$

$$+ 2n(2n+1) \frac{K}{b} \left\{ \frac{\left(\frac{b}{a}\right)^{4n+1} - 1}{(2n+1)\left(\frac{b}{a}\right)^{4n+1} + 2n} \right\},$$

$$M_{2,n} = \frac{4K}{a^2 \delta^2} \sum_{s=0}^{\infty} \frac{\left[ \frac{\partial}{\partial r} B_{2n+\frac{1}{2}}(\sigma_s, r) \right]_{r=b}}{\sigma_s^5 \frac{\partial}{\partial \sigma_s} B_{2n+\frac{1}{2}}(\sigma_s, b)} \left\{ 2 - 3e^{-\sigma_s^2 a \delta} + e^{-2\sigma_s^2 a \delta} - \sigma_s^2 a \delta \right\} \quad (15)$$

$$+ 2n(2n+1) \frac{K}{b} \left\{ \frac{\left(\frac{b}{a}\right)^{4n+1} - 1}{(2n+1)\left(\frac{b}{a}\right)^{4n+1} + 2n} \right\},$$

and

$$M_{m-r+1, n} = -\frac{4K}{a^2 \delta^2} \sum_{s=0}^{\infty} \frac{\left[ \frac{\partial}{\partial r} B_{2n+\frac{1}{2}}(\sigma_s, r) \right]_{r=b}}{\sigma_s^5 \frac{\partial}{\partial \sigma_s} B_{2n+\frac{1}{2}}(\sigma_s, b)} e^{-\sigma_s^2 a(m-r+1) \delta} \left( e^{\sigma_s^2 a \delta} - 1 \right)^3 \quad (16)$$

for  $m-r+1 > 2$ .

The evaluation of  $B_{2n+\frac{1}{2}}(\sigma_s, r)$ , its first derivatives with respect to  $r$  and  $\sigma_s$ , and its zeros, is given in detail in references (4) and (9). In reference (6) a Fortran II computer program is described for the inverse problem of the heated shell using the wall-splitting technique. Reference (9) describes another computer program for calculating the surface temperature and heat input to a hemispherical shell from a prescribed outer surface variation of heat transfer coefficient and recovery temperature.

## 4. RESULTS AND DISCUSSION

The raw temperature data measured by each of the nineteen thermocouples is shown in figures 7 to 14. All the data except that measured at the three stations for  $\theta=20^\circ$  is compatible with axisymmetric flow around the hemisphere. When, as is shown in figure 11, the temperature measurements for  $\phi=0, \theta=20^\circ$ , are superimposed on those for  $\phi=120^\circ, \theta=20^\circ$ , a marked difference is apparent. The temperatures at  $\phi=0$  rise more steeply than those for  $\phi=120^\circ$ . The incidence required to account for such a temperature difference would be more than the rocket vehicle could withstand and the thermocouple at  $\phi=0, \theta=20^\circ$ , was checked in the laboratory after the trial and found to be in perfect working order. This then leaves boundary layer transition as an explanation. Earlier boundary layer transition in the  $\phi=0$  meridian plane than in the  $\phi=\pm 120^\circ$  planes due perhaps to different surface roughness distributions is in keeping with observed boundary layer behaviour on hemispherical noses. There is also some discernible difference between the temperature measurements for  $\phi=120^\circ$  and  $\phi=-120^\circ$  at  $\theta=20^\circ$  and although this difference is not nearly so marked it does lend weight to the assumption that asymmetric boundary layer transition occurred in the neighbourhood of  $\theta=20^\circ$ .

For the purpose of smoothing, each record of measured temperatures was represented by a Fourier sine series fitted about a straight line. Plots of the logarithm of amplitude against frequency are shown for the Fourier terms representing the temperatures measured at  $\phi=120^\circ, \theta=20^\circ, 30^\circ, 40^\circ$  in figures 16, 17 and 18. Similar plots were obtained for all the other measurements and they serve to show the range of amplitude values dominated by noise and the range which is predominantly signal. From the amplitudes representing the noise, standard deviations for the noise in the Fourier coefficients have been calculated and cut-off frequencies for smoothing were chosen such that only those frequencies having amplitudes which exceeded six standard deviations were retained. As a result the standard deviation of the error due to noise in the raw data among the nineteen records varied between  $5.5^\circ\text{K}$  and  $8.6^\circ\text{K}$ , whereas the standard deviation of the error in the smoothed data varied between  $0.49^\circ\text{K}$  and  $0.82^\circ\text{K}$  when Fourier terms with amplitudes less than  $0.52^\circ\text{K}$  were rejected. Bias errors were found to be quite small having a maximum value of order  $0.5^\circ\text{K}$ . Two examples of curves of Fourier smoothed temperatures superimposed on raw data are shown in figures 19 and 20. Most of the noise seems to occur in the last two seconds of each record when ablating silicon rubber used as thermal protection could have passed on to the surface of the telemetry transmitting aerials.

The smoothed temperatures were represented by

$$\sum_{n=0}^{n=6} \tilde{T}_{2n}(a, t) P_{2n}(\cos \theta),$$

the first seven terms of their Legendre polynomial expansions. Just how well these first seven terms represent the smoothed temperatures can be seen from figures 19 and 20. The worst fit occurred for  $\phi=120^\circ, \theta=30^\circ$ , as shown in figure 19 and the result for  $\phi=-120^\circ, \theta=30^\circ$ , was much the same. However, the representation for all the other data displayed the same quality of fit as shown for  $\phi=0, \theta=50^\circ, 70^\circ, 90^\circ$ , in figure 20, including  $\phi=0, \theta=30^\circ$ . This raises the question of just how many terms are needed in the Legendre polynomial expansions. Certainly the seven terms used seem adequate for all but the  $\phi=\pm 120^\circ, \theta=30^\circ$  cases where it might be expected that adding about two more terms would greatly improve the representation. Where a fairly large number of terms is needed, this suggests that instead of truncating the infinite series it would be worthwhile to assume a finite expansion in the first place and find the Legendre coefficients from a system of simultaneous algebraic equations such that the smoothed thermocouple readings are regenerated exactly. This process would be much simpler than calculating the exact Legendre coefficients through their integral representations as defined for example by equation (2). The disadvantage would be that the Legendre coefficients found from the finite expansions would not be exact but they do have the useful property that

their error diminishes as the number of terms in the finite expansion increases. Even in attempting to find the exact coefficients there will be errors arising from the integration of products of  $\cos^n \theta$  and a function represented numerically or approximated by a series of suitably simple analytic functions. Before performing another heating experiment in this way on a hemisphere it would be worthwhile carrying out an accuracy check on the orders of finite Legendre polynomial expansions required to represent analytical descriptions of typical temperature profiles to within given accuracies.

From the values of  $\tilde{T}_{2n}(a,t)$  the Legendre coefficients,  $\tilde{T}_{2n}(b,t)$ , of the outer surface temperature were calculated through equation (7), employing the wall-splitting technique where necessary, and the reconstituted outer surface temperatures given by

$$T(\cos \theta, b, t) = \sum_{n=0}^{n=6} \tilde{T}_{2n}(b, t) P_{2n}(\cos \theta)$$

are shown plotted in figures 21, 22 and 23. Each row of thermocouples along  $\phi = \pm 120^\circ$  and  $\phi = 0$  was treated independently and no attempt has been made to use the fact that the stagnation point thermocouple was common to each array and consequently the differences in the derived values of  $T(b,t)$  at  $\theta = 0$  for the three values of  $\phi$  serve as an indication of the error in the method. The agreement between  $T(b,t)$  at the stagnation point for  $\phi = 120^\circ$  and  $\phi = -120^\circ$  is quite good whereas the agreement of these with  $\phi = 0$  is not so good. As shown in figure 11 the raw temperature data profile for  $\phi = 0$  rises more steeply than that for  $\phi = 120^\circ$  at  $\theta = 20^\circ$  and the different profile has produced different values for the Legendre coefficients of which only seven have been used to reconstitute temperature. This is where the alternative finite Legendre expansion proposed in the previous paragraph would have ensured a value of  $T(a,t)$  at the stagnation point common to each row. The steeper rise in the raw temperature data for  $\phi = 0$ ,  $\theta = 20^\circ$ , is reflected in the outer surface temperature profiles of figure 21 when compared against the profiles for  $\phi = 120^\circ$  in figures 22 and 23. Another feature is the oscillation that occurs in some of these temperature profiles after the temperatures pass through their maximum values. This oscillation is undoubtedly a result of the Legendre representation by seven terms where the last term retained includes a  $\cos \theta$  to the twelfth power which therefore has a  $\cos 12 \theta$  component with a period of  $30^\circ$ . The oscillation does have a period of roughly  $30^\circ$  and manifests itself as a sort of relaxation effect due to the incomplete Legendre expansion attempting to represent the sudden ending of a steep temperature rise. The amplitude is small enough to be able to put a mean curve through each oscillation and the temperature values read for each mean would only vary by a few per cent from those corresponding to the oscillation. Such oscillations are typical of those which can occur when a rapidly changing function is represented by the first few terms of its Fourier expansion. It is possible to improve the convergence of Fourier series and hence get better results with fewer terms by using the so-called sigma factors to modify the values of the Fourier coefficients. If necessary these sigma factors could be used to smooth out oscillations in the Legendre representations and this would provide an objective means for introducing the mean curves.

Having left these oscillations without any smoothing in the outer surface temperature profiles, it is not surprising that they reappear in the derived heat transfer profiles as shown in figures 24 to 29. Here again the amplitudes are small and there is not much difficulty in guessing at positions for mean curves. Outer surface heat transfer,  $Q_r(b,t)$  was derived from the time histories of the Legendre components of outer surface temperature,  $\tilde{T}_{2n}(b,t)$ , through use of equation (13). Apart from the heat transfer profiles for time 8 seconds and above, where the raw data is noisy, there is reasonable agreement between the profiles over the rear part of the hemisphere for the three meridian planes  $\phi = \pm 120^\circ$  and  $\phi = 0$ . However,

over the front part of the hemisphere there are marked differences in the heat transfer profiles shown in figures 24 to 29 and the question is, how authentic are these differences? This question is important in deciding where boundary layer transition occurred. The initial heat transfer profile shapes are strongly influenced by the levels of heat transfer at  $\theta=0$  and  $\theta=20^\circ$  which were the positions at which temperature data was recorded. The curves joining the points  $\theta=0$  and  $\theta=20^\circ$  are Legendre polynomial interpolations which also take into account the data recorded from all the other thermocouples in the same row. A guide to the authenticity of the derived heat transfer differences at  $\theta=20^\circ$  between the three meridian planes  $\phi = \pm 120^\circ$  and  $\phi=0$  can be obtained by comparing heat transfer variation with time against the time-derivative variations for the smoothed inner face temperature measurements. The temperature profiles of figures 21, 22 and 23, show only slight curvature at  $\theta=20^\circ$  and hence most of the local temperature rise is due to aerodynamic heat input rather than circumferential heat conduction and there should thus be a correlation between the time-derivative of the inner face temperature,  $\frac{dT}{dt}(a,t)$ , and the aerodynamic heat transfer  $Q_r(b,t)$ . That there is such a correlation can be seen from figure 30 and this means that the differences in the derived heat transfer results for  $\theta=20^\circ$  are reflected in the raw temperature measurements. The scatter in the derived heat transfer results for the stagnation point,  $\theta=0$ , is shown in figure 31. Three different results for stagnation point heat transfer were derived because each row of thermocouples was treated independently. The scatter can thus be regarded as indicating the accuracy of truncating the Legendre polynomial expansions of temperature at the seventh term. It appears from figure 31, that the markedly different profile of the measured temperature at  $\phi=0$ ,  $\theta=20^\circ$ , has carried through to the  $\phi=0$ ,  $\theta=0$ , profile, which is seen to account for most of the scatter up to about 6.5 seconds. In the light of these observations we can now re-examine the initial heat transfer profiles of figures 24 to 29 and draw some conclusions about transition. Up to time 4 seconds, figures 24, 25 and 26, all exhibit a characteristic laminar heating profile up to about  $\theta=15^\circ$ . At time 5 seconds, figures 24 and 26 show profiles for  $\phi=0$  and  $\phi=-120^\circ$  which indicate transition to turbulent flow very close to the stagnation point. This situation appears to exist up to time 6 seconds, if the possibility of a lower value of  $Q_r(b,t)$  than that shown in figure 26 for  $\phi=-120^\circ$ ,  $\theta=0$ , is accepted in accordance with the amount of scatter present at time 6 seconds, shown in figure 31. For  $\phi=-120^\circ$ , figure 29 shows a strong tendency for the flow to revert to transition at about  $\theta=15^\circ$  for time 6.4 seconds, even if some account is taken of possible scatter. For time 7 seconds and above, it appears from figures 27, 28 and 29, that the flow becomes fully turbulent at about  $\theta=20^\circ$ .

It is really more appropriate to look at Stanton number variations when drawing conclusions about transition. Stanton number variations are shown in figures 32 to 37. These figures tend to support the conclusions drawn from the heat transfer profiles of figures 24 to 29 and the initial laminar profiles for times less than 8 seconds in figure 37 for  $\phi=-120^\circ$  are more pronounced than their heat transfer counterparts in figure 29. The two Stanton number profiles for times of 8 seconds are greatly distorted versions of their heat transfer counterparts because at these times the difference between the outer surface temperature and recovery temperature rapidly becomes small and has the effect of magnifying oscillations when divided into the heat transfer to obtain Stanton number. Also, the Stanton number based on the difference between recovery temperature and outer surface temperature or wall temperature,  $T_r - T_w$ , stems from steady flow theory whereas in the transient case with a falling recovery temperature the heat transfer to the outer surface will not have reached zero by the time  $T_r$  falls to  $T_w$ . Hence, near this condition, the Stanton number tends to infinity. Rough calculations show the temperature response time for the boundary layer well back on the hemisphere to be of order 30 milliseconds at time 8 seconds. A comparison between the derived Stanton numbers for the stagnation point and those for the steady

laminar flow stagnation point theory developed from reference 10 and described in reference 11 is shown in figure 38. In figure 39 the stagnation point heat transfer calculated from this laminar theory is compared with the derived values treating each row of thermocouples separately. Agreement is seen to be good except for about one and a half seconds past maximum heating where the derived values are up to twenty five per cent higher than laminar steady flow theory.

Values for maximum turbulent heating around a hemisphere are of interest because they are difficult to predict. An envelope of maximum turbulent Stanton number values, taken from the heating profiles around the hemisphere for the three meridian planes, is shown in figure 40. These maxima occur at about  $30^\circ$  from stagnation point initially, shifting backwards towards  $60^\circ$  as the hemisphere becomes hot. In this experiment the maximum turbulent Stanton numbers ranged from 0.0022 to 0.0037.

## 5. CONCLUSIONS

Outer surface temperature and heat transfer profiles have been deduced from inner surface measurements of the temperature in a hemispherical shell which reached a Mach number of 5.5 at 4 km altitude after 7 seconds of flight. In deducing outer surface conditions a new mathematical technique has been tested and found to have been effective. In any future experiment using this technique it is recommended that at least nine equally spaced thermocouples per row, in addition to the one at the stagnation point, be used, and that finite Legendre expansions having the same number of terms as the number of thermocouples in a row be fitted to the measurements by solving the resulting simultaneous algebraic equations for the coefficients. This avoids the difficulty of having to perform numerical integration of oscillatory functions.

The derived heat transfer profiles are characteristic of a boundary layer flow which is laminar in the stagnation region and undergoes transition to turbulent flow within the first  $20^\circ$  of arc. Agreement with laminar stagnation point heat transfer theory for steady flow is good except for just after maximum heating where the results from the experiment are up to some 25 per cent higher. Maximum turbulent heat transfer occurred between  $30^\circ$  and  $60^\circ$  from the stagnation point with maximum values of Stanton number ranging from 0.0022 to 0.0037.

## 6. ACKNOWLEDGEMENTS

The research program, of which this experiment was part, suddenly found itself overtaken by higher priority work and consequently the writing of a formal report became delayed. Since 1971, when this experiment was conducted, the responsibility for preparing the report changed hands several times and finally rested with the present author who wishes to acknowledge the contributions made by others. The major contribution to be acknowledged was made by Mr I.C. Heron of Aerodynamics Research Group who adapted to hemispherical shells, the techniques used for flat plates, and developed the computer programs needed to carry out the numerical analysis. Also to be acknowledged is the contribution made by Dr R.L. Pope of Dynamics Group who performed the Fourier smoothing and error analysis of the raw data. Finally, the work performed by the staff of Field Experiments Group must be acknowledged in painstakingly welding the thermocouples to the hemisphere, in building the instrumentation, and in preparing and firing the rocket vehicle.

NOTATION

a	inner radius of hemispherical shell
b	outer radius of hemispherical shell
l	thickness of a flat plate conductor
m,n	integers
P	operational transform of time t
r	radial coordinate in shell or an integer
s	an integer
t	time
x	distance coordinate in a flat plate conductor
$B_{2n+1/2}$	function of Spherical Bessel Functions of the first and second kinds defined by equation (6)
$C_p$	specific heat of air at constant pressure
K	coefficient of thermal conductivity for hemispherical shell
M	memory coefficient defined by equations (14), (15), (16)
$P_{2n}$	Legendre polynomial of order 2n
Q	rate of heat flow per unit area
$Q_r$	rate of heat flow per unit area in radial direction
$Re_D$	Reynolds number based on shell diameter
$S_t$	Stanton number = $Q_r / \rho U C_p (T_r - T_w)$
T	temperature
$T_r$	recovery temperature
$T_w$	wall heated surface temperature
U	free stream velocity
z	argument used for Spherical Bessel Functions
$\alpha$	thermal diffusivity
$\delta$	time increment

$\theta$	angle in shell coordinate system shown in figure 15
$\mu$	$\cos \theta$
$\xi, \xi_1$	dummy time variables
$\rho$	air density
$\sigma_s$	the sth zero of B
$\phi$	angle of meridian plane for a thermocouple array as shown in figure 6
$\Theta$	temperature memory coefficient as defined by equations (8) and (9)
Subscripts	
$\infty$	free stream conditions

REFERENCES

No.	Author	Title
1	Jepps, G. Heron, I.C. Evans, H.W.	"Proposal for a Free-Flight Experiment on the Aerodynamic Heating of a Hemispherical Shell". WRE-TM-HSA 199, October 1969
2	Carslaw, H.W. Jaeger, J.C.	"Conduction of Heat in Solids". Oxford Clarendon Press, 1959
3	Abramowitz, M. Stegun, I.A.	"Handbook of Mathematical Functions". Dover Publications, 1965
4	Heron, I.C.	"Heat Conduction in Hemispherical Shells with Applications to Aerodynamic Heating". WRE-TN-HSA 124, April 1967
5	Jepps, G.	"Heat Conduction in Single-Layer and Double-Layer Walls, with Boundary Conditions Appropriate to Aerodynamic Heating". Australian Aeronautical Research Committee Report ACA-66, November 1965
6	Heron, I.C.	"A Method for Removing Numerical Instability from the Solution of the Inverse Thick-Shell Heating Problem". WRE-TN-HSA 139, December 1968
7	Pope, R.L.	"Noise Amplification During Analysis of Aerodynamic Heating Experiments". WRE-TN-1575 (WR&D), March 1976
8	Heron, I.C.	"An Evaluation of Errors that Occur in the Solution of the Inverse Heating Problem for Flat Plates and Hemispherical Shells". WRE-TN-HSA 188, November 1970
9	Heron, I.C.	"A Fortran Program for Predicting the Temperature-Time Histories of Hemispherical Shells Subjected to Aerodynamic Heating". WRE-TN-783 (WR&D), October 1972
10	Fay, J.A. Ridell, F.R.	"Theory of Stagnation Point Heat Transfer in Dissociated Air". J. Aero. Sc. Vol. 25 No.2 p.73, February 1958
11	Crabtree, L.R. Dommett, R.L. Woodley, J.G.	"Estimation of Heat Transfer to Flat Plates, Cones and Blunt Bodies". RAE-TR-65137, July 1965

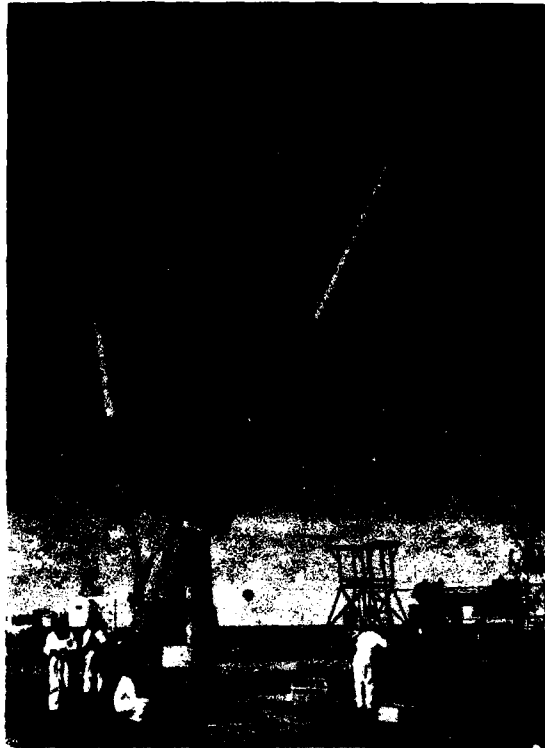
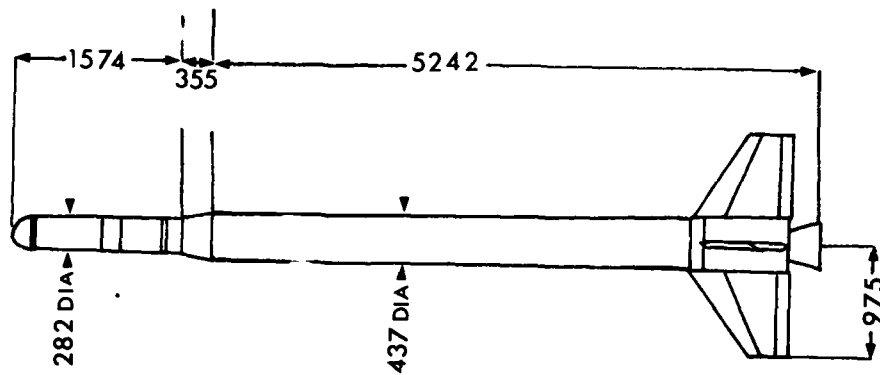


Figure 1. Photograph of rocket test vehicle on launcher



(All dimensions in mm)

2. Sketch of rocket test vehicle

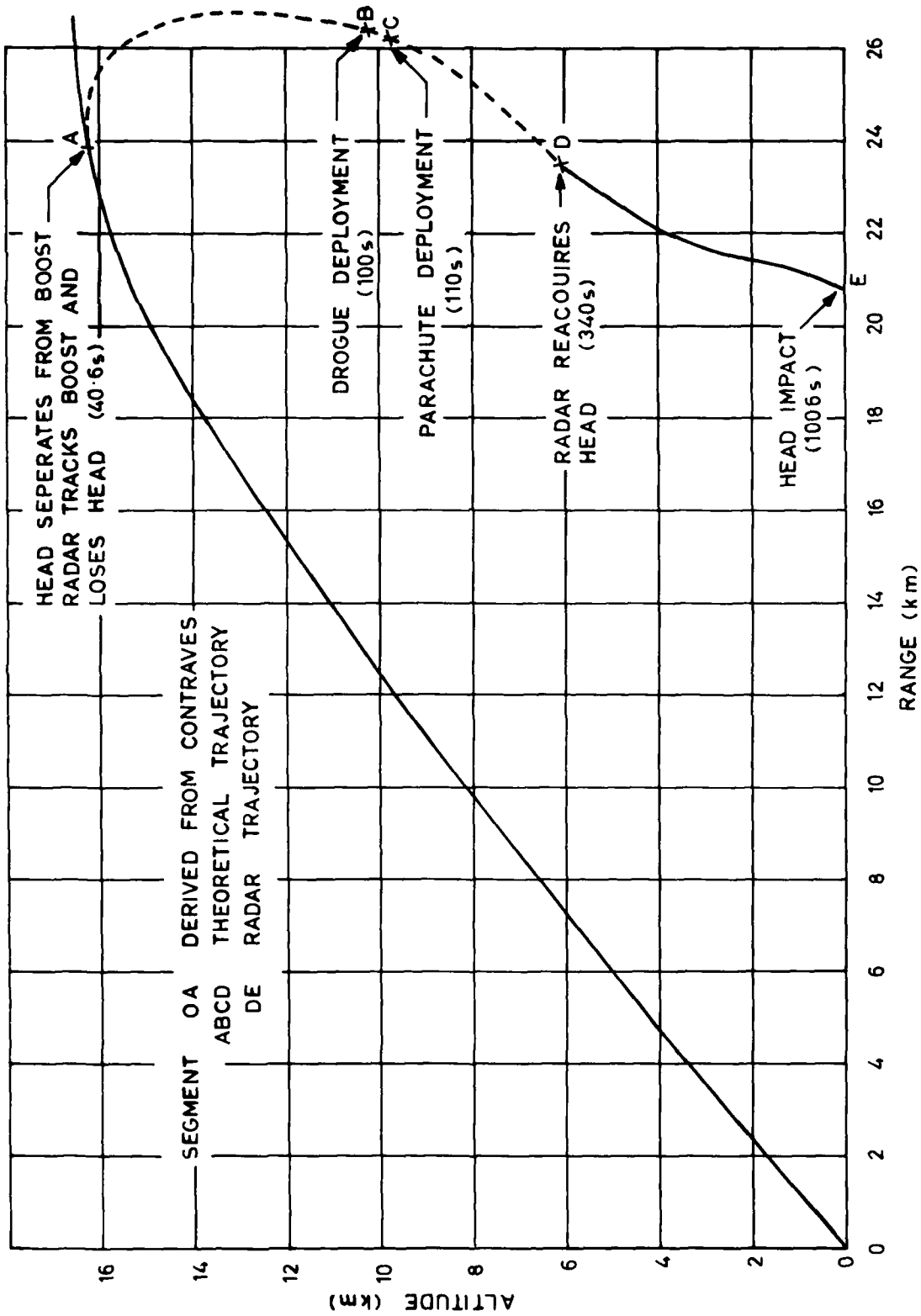


Figure 3. Flight path showing recovery events

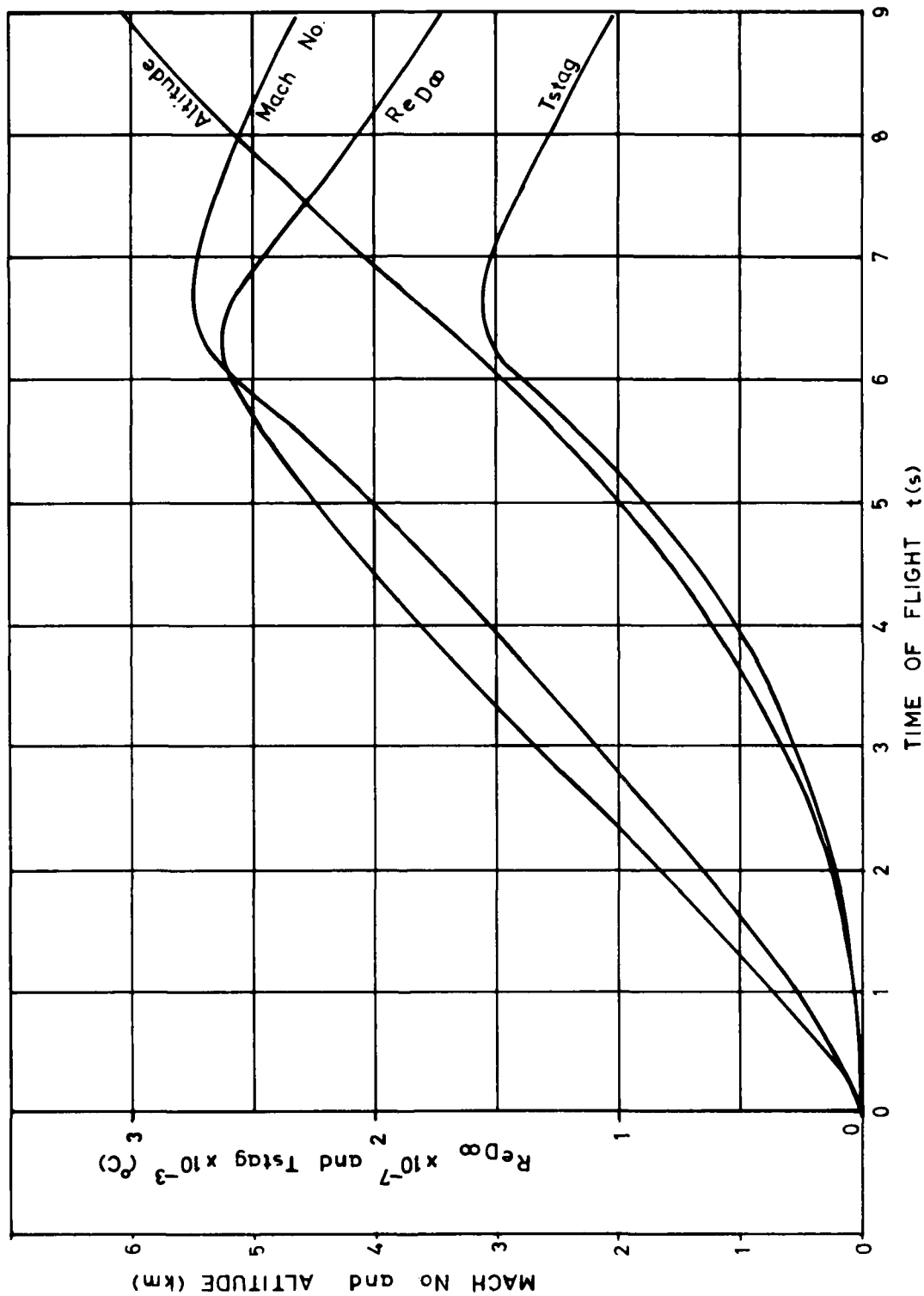


Figure 4. Mach number, free stream Reynolds number, altitude, and stagnation temperature histories

WSRL-0069-TR  
Figure 5



Figure 5. Photograph of hemisphere and instrumentation compartment just after impact

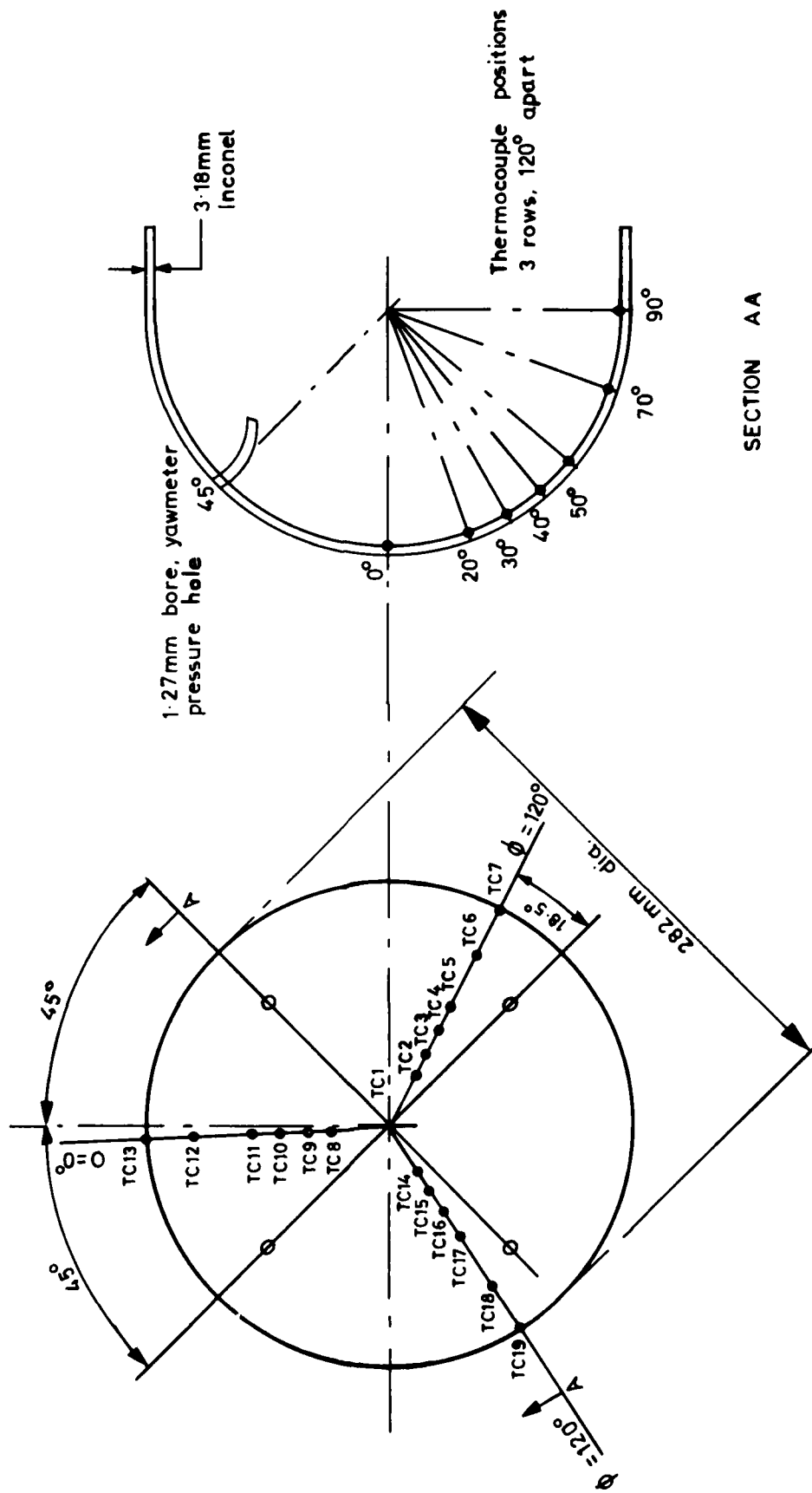


Figure 6. Positions of thermocouples and differential pressure yawmeter holes

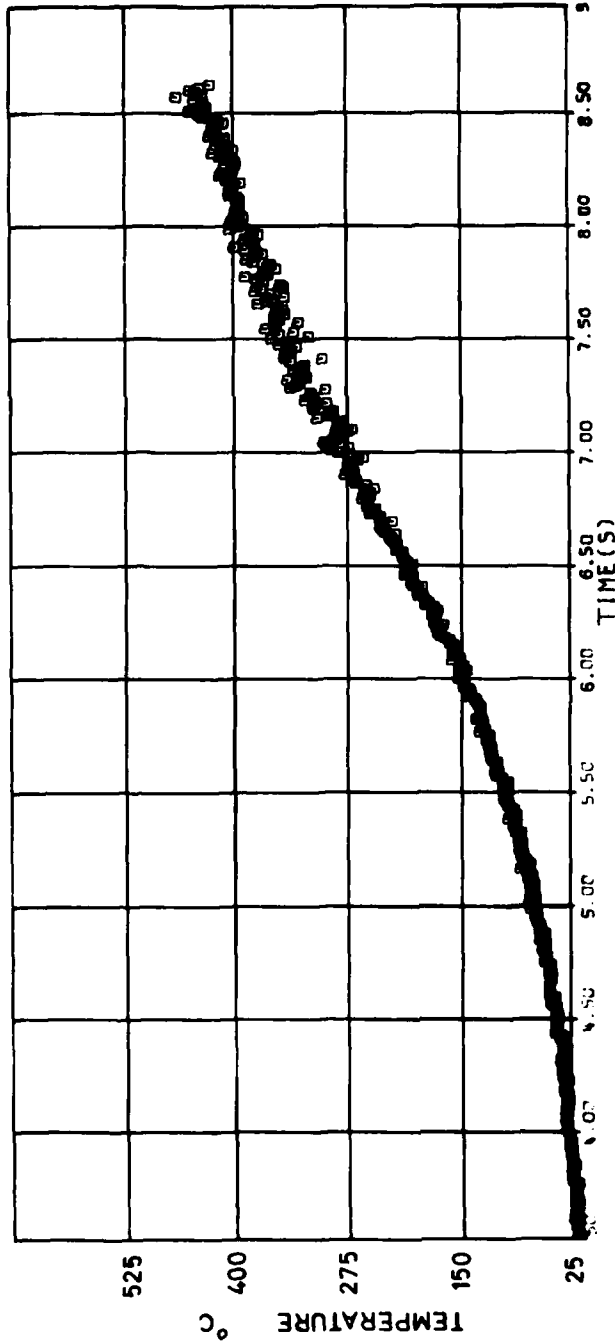


Figure 7. Raw temperature measurements (stagnation point  $\theta=0$ )

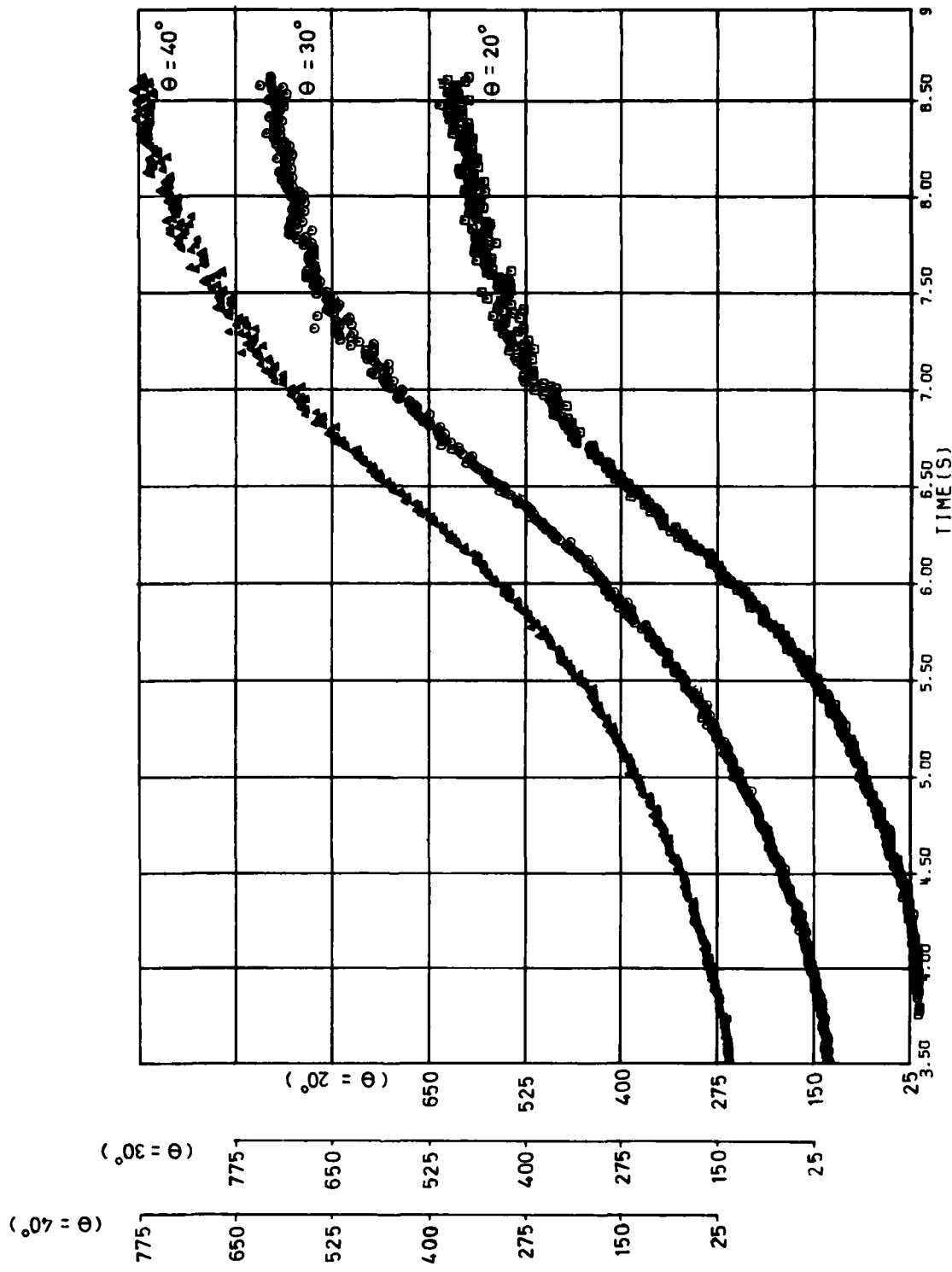


Figure 8. Raw temperature measurements ( $\phi=0^\circ$ ,  $\theta=20^\circ$ ,  $30^\circ$ ,  $40^\circ$ )

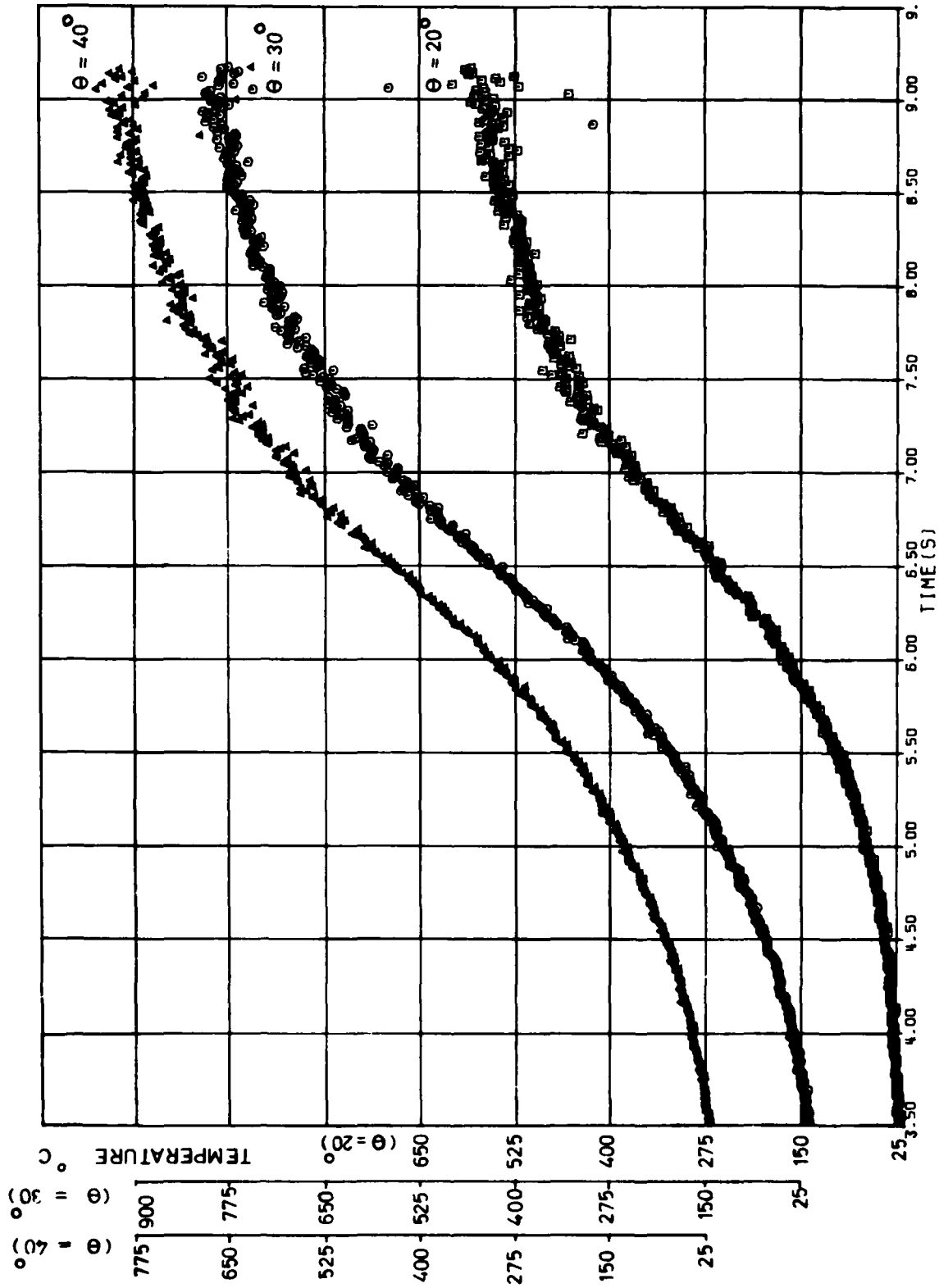


Figure 9. Raw temperature measurements ( $\phi=120^\circ$ ,  $\theta=20^\circ$ ,  $30^\circ$ ,  $40^\circ$ )

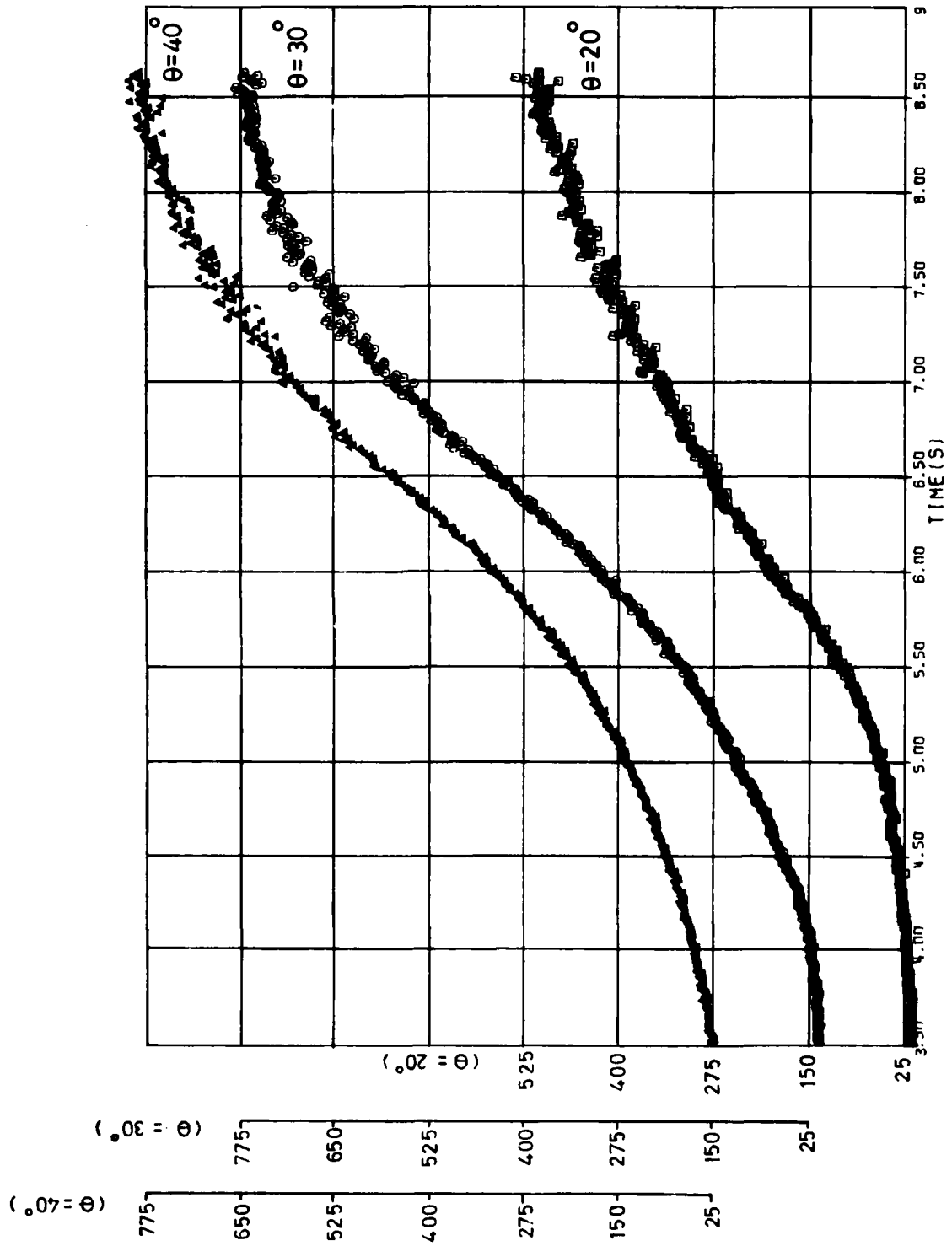


Figure 10. Raw temperature measurements ( $\phi = -120^\circ$ ,  $\theta = 20^\circ$ ,  $30^\circ$ ,  $40^\circ$ )

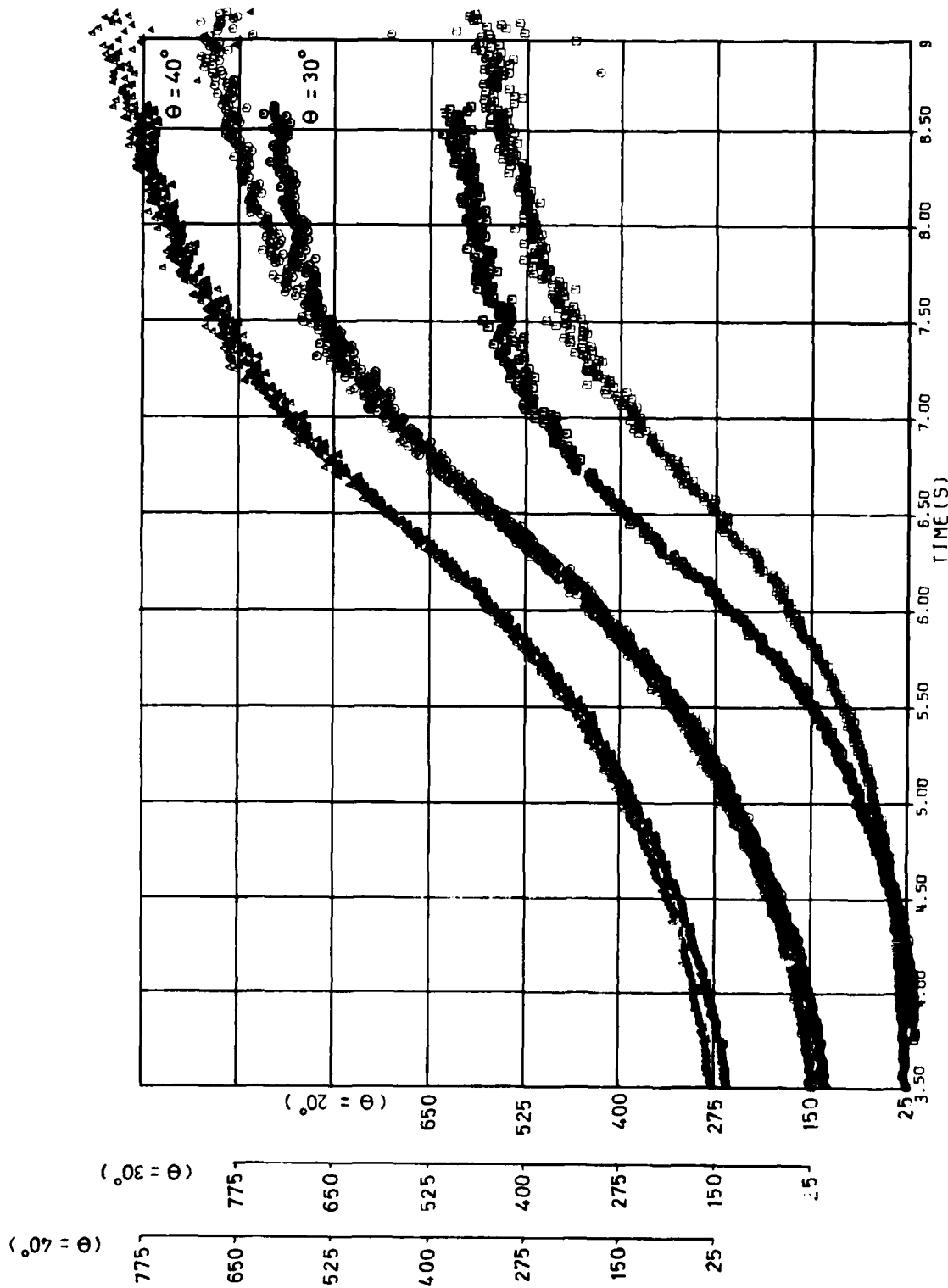


Figure 11. Raw temperature measurements (superpositioning of  $\phi=0$  upon  $\phi=120^\circ$  for  $\theta=20^\circ, 30^\circ, 40^\circ$ )

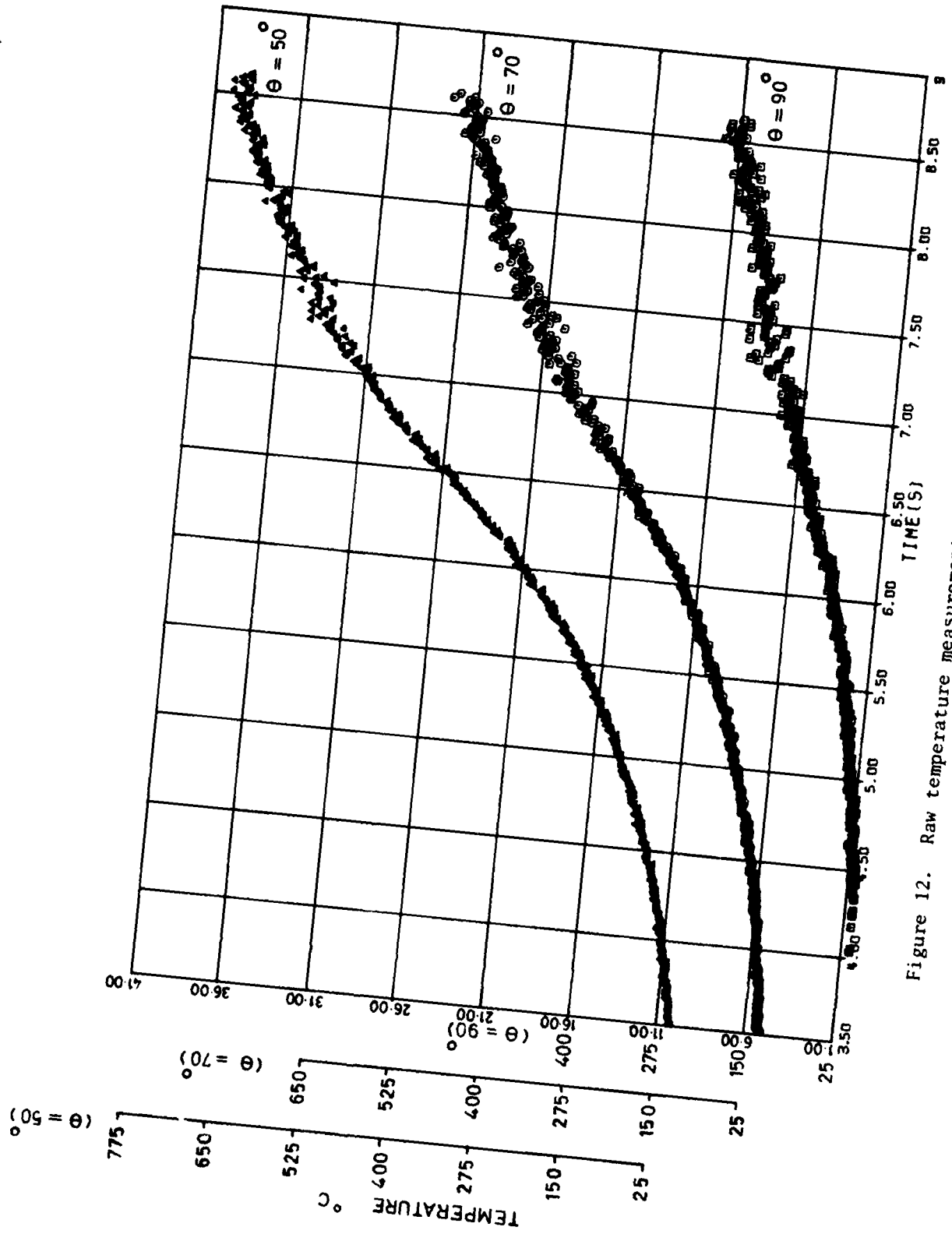


Figure 12. Raw temperature measurements ( $\phi=0$ ,  $\theta=50^\circ$ ,  $70^\circ$ ,  $90^\circ$ )

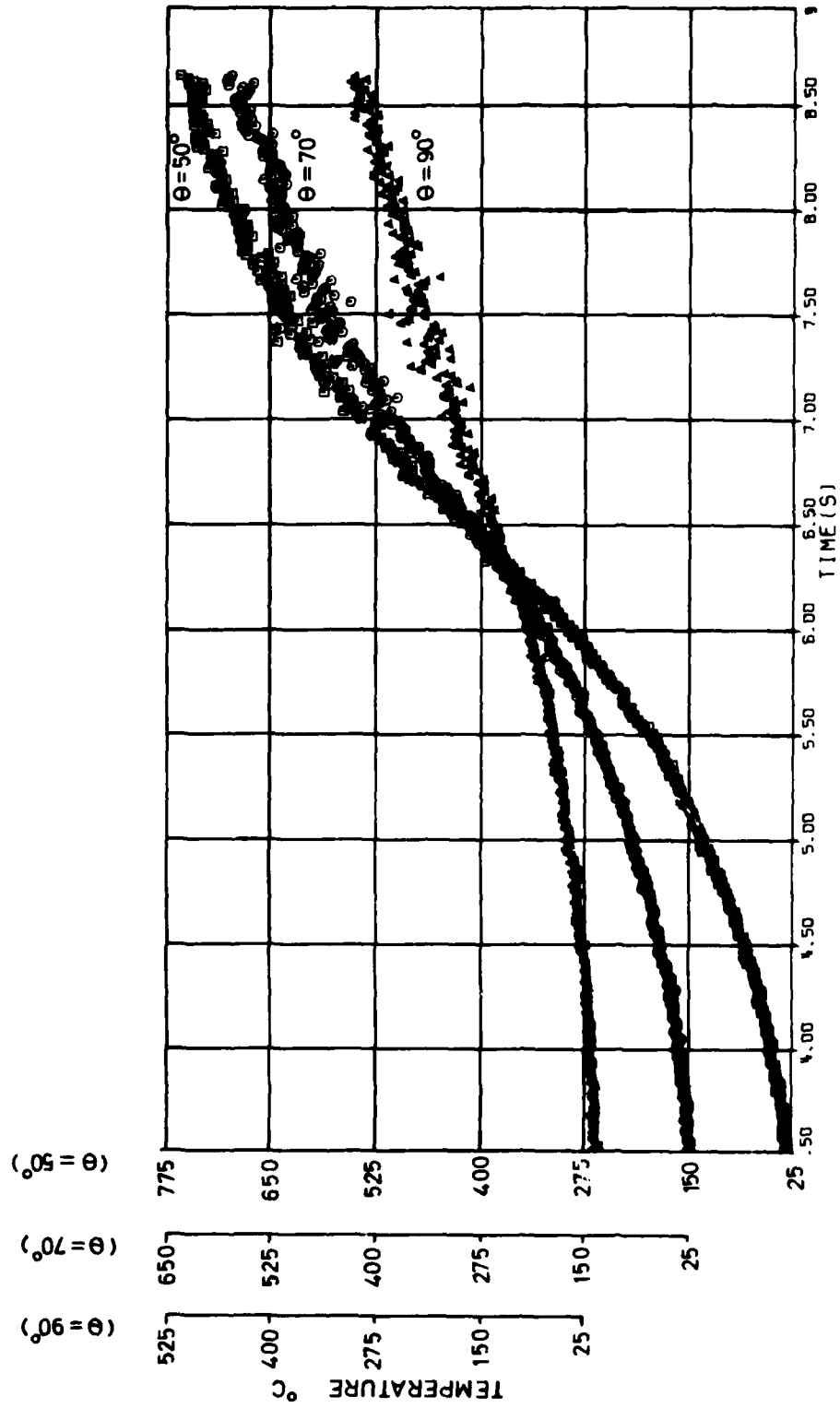


Figure 13. Raw temperature measurements ( $\phi=120^\circ$ ,  $\theta=50^\circ$ ,  $70^\circ$ ,  $90^\circ$ )

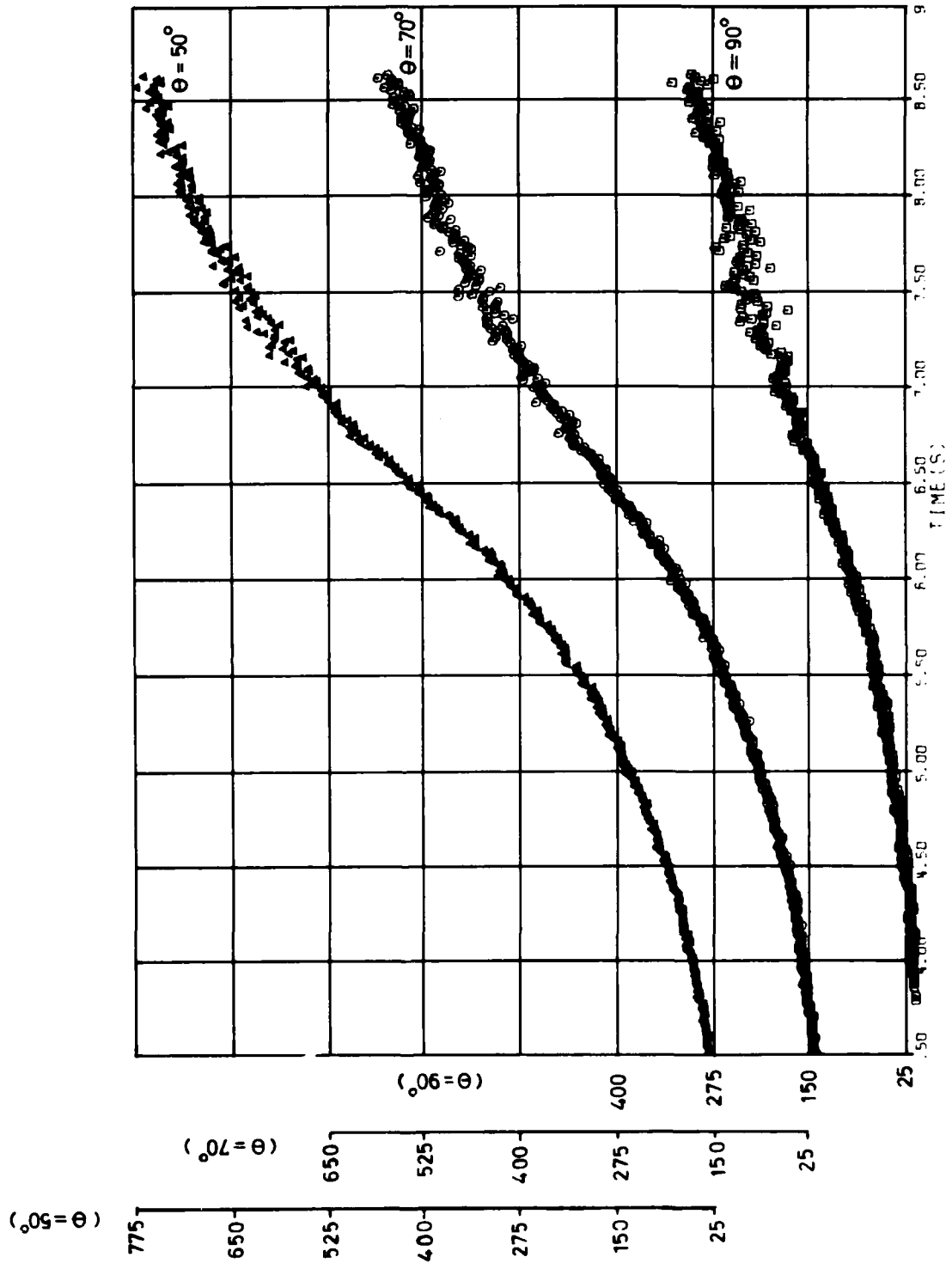


Figure 14. Raw temperature measurements ( $\phi = -120^\circ, \theta = 50^\circ, 70^\circ, 90^\circ$ )

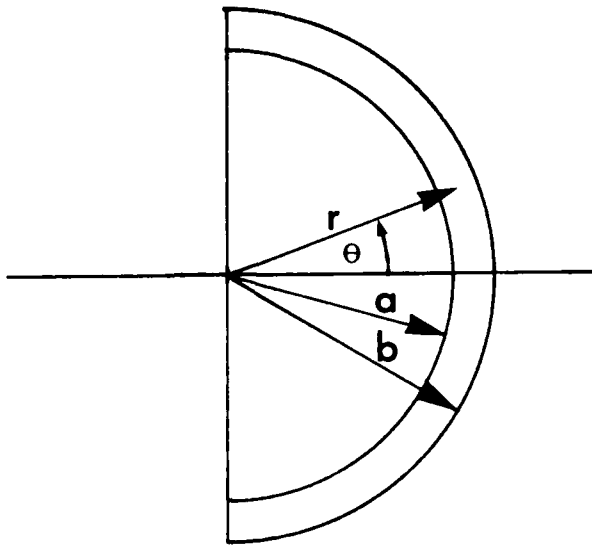


Figure 15. Coordinate system for hemispherical shell

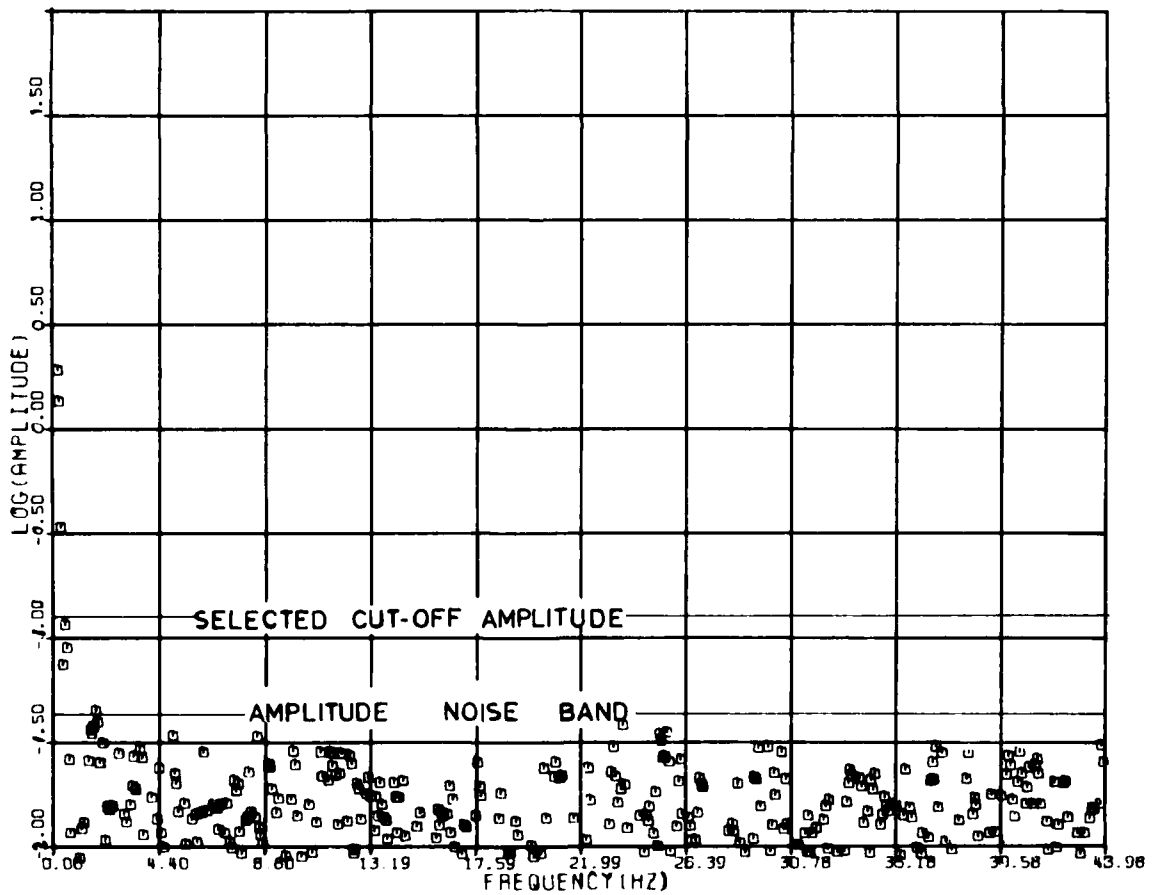


Figure 16. Amplitude and frequency of the Fourier components of temperature  
( $\phi=120^\circ$ ,  $\theta=20^\circ$ )

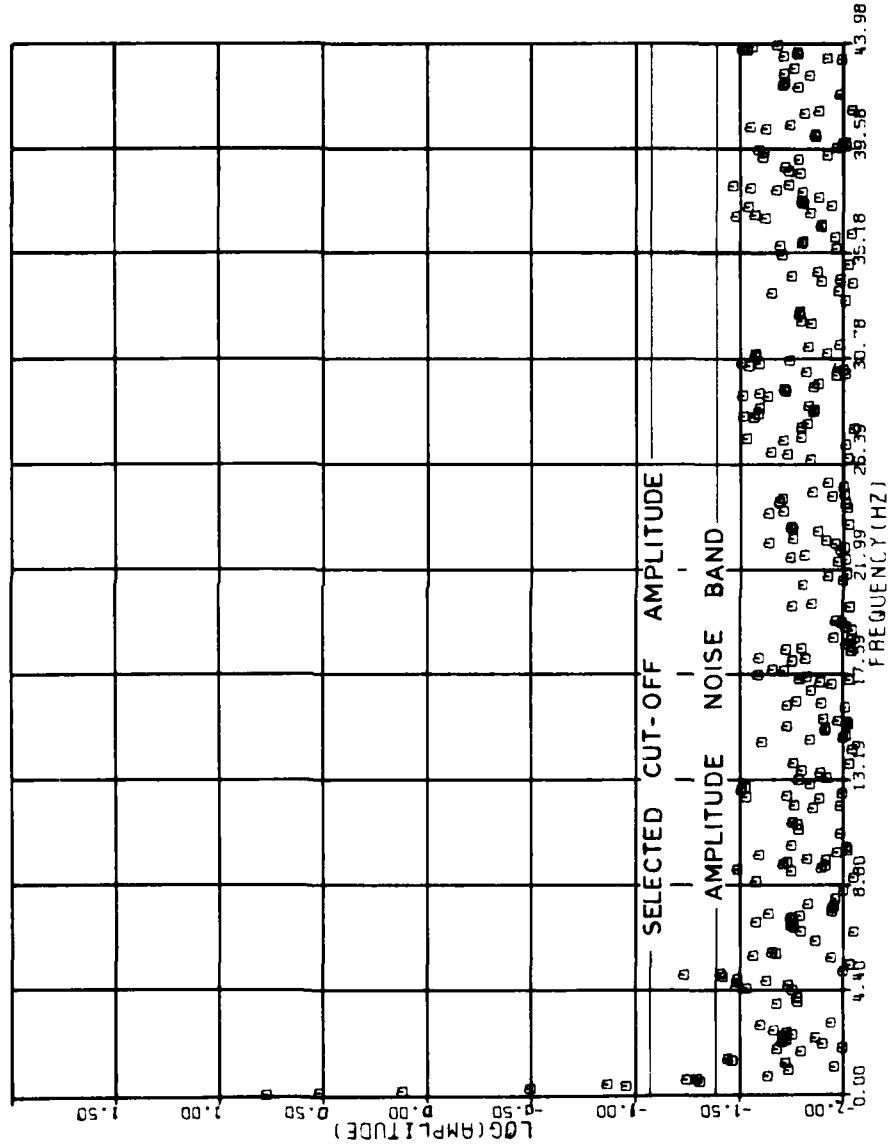


Figure 17. Amplitude and frequency of the Fourier components of temperature ( $\phi=120^\circ$ ,  $\theta=30^\circ$ )

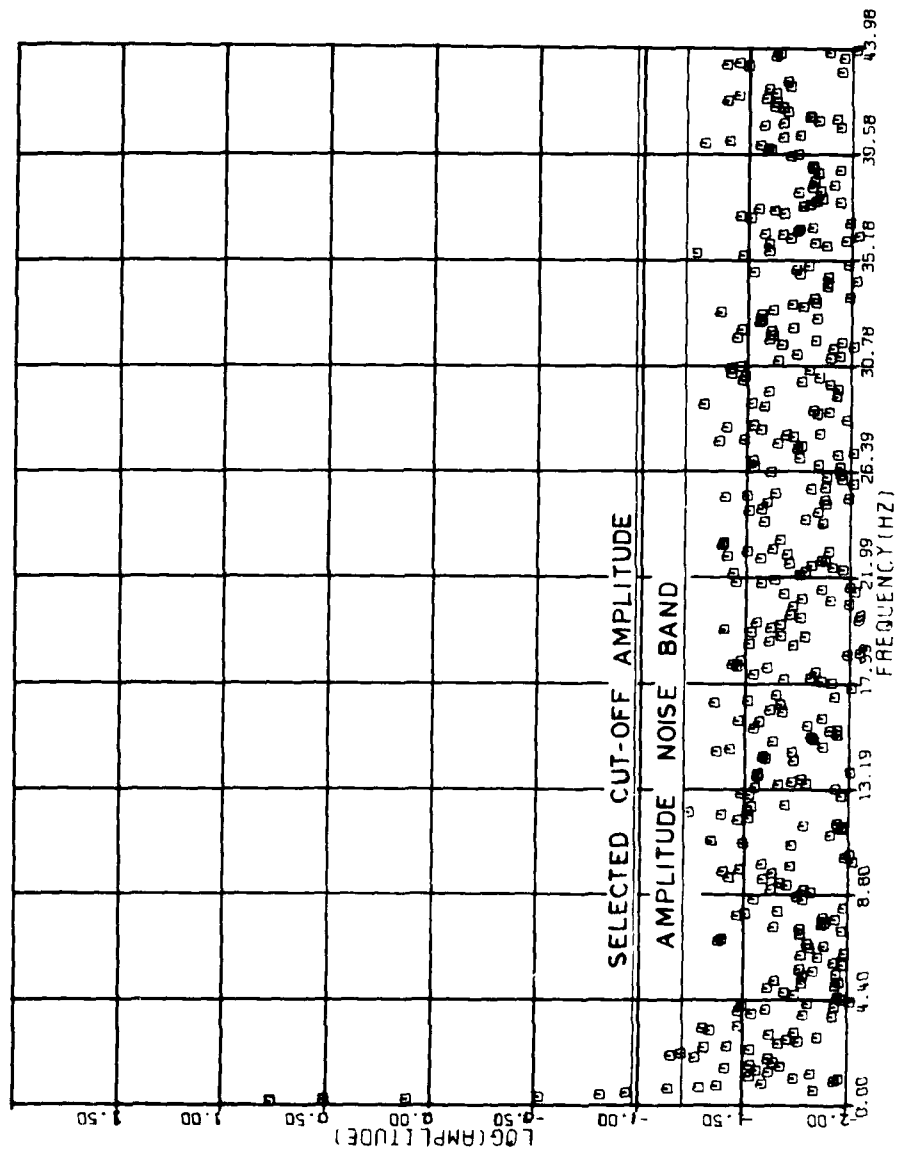


Figure 18. Amplitude and frequency of the Fourier components of temperature ( $\phi=120^\circ$ ,  $\theta=40^\circ$ )

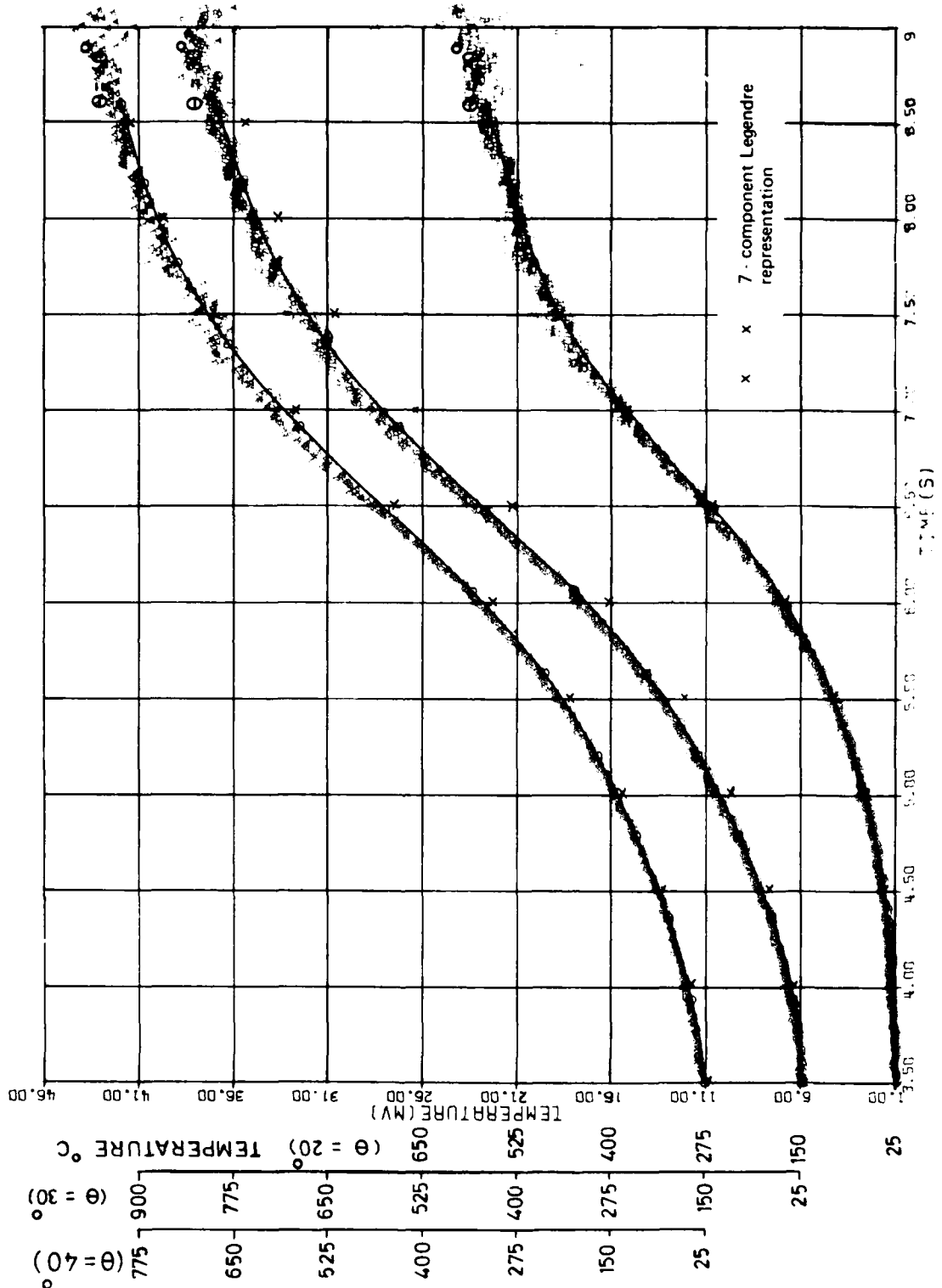


Figure 19. Fourier smoothed and seven-component Legendre temperature representation superimposed on raw data ( $\phi=120^\circ$ ,  $\theta=20^\circ$ ,  $30^\circ$ ,  $40^\circ$ )

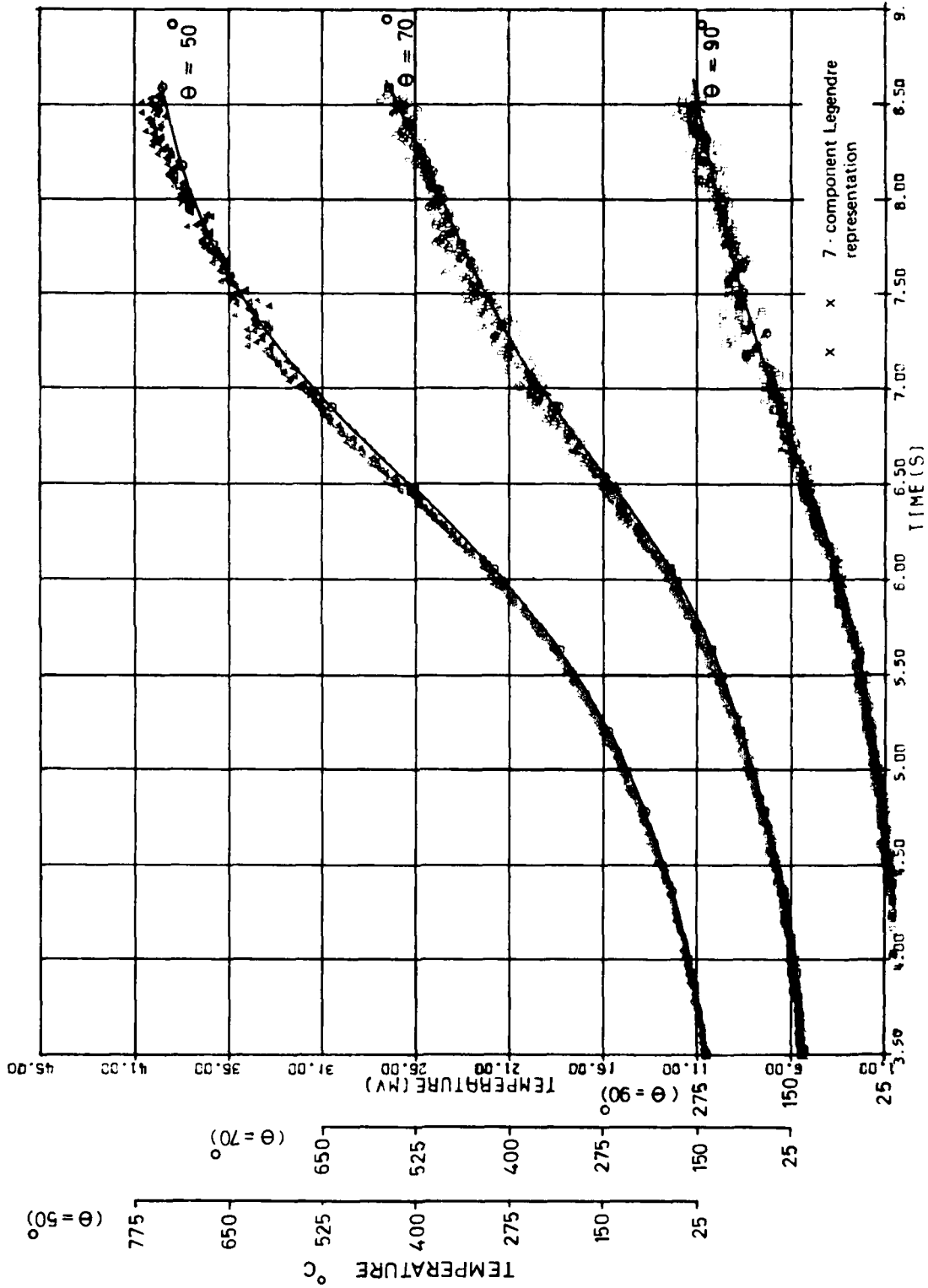


Figure 20. Fourier smoothed and seven-component Legendre temperature representation superimposed on raw data ( $\phi=0$ ,  $\theta=50^\circ$ ,  $70^\circ$ ,  $90^\circ$ )

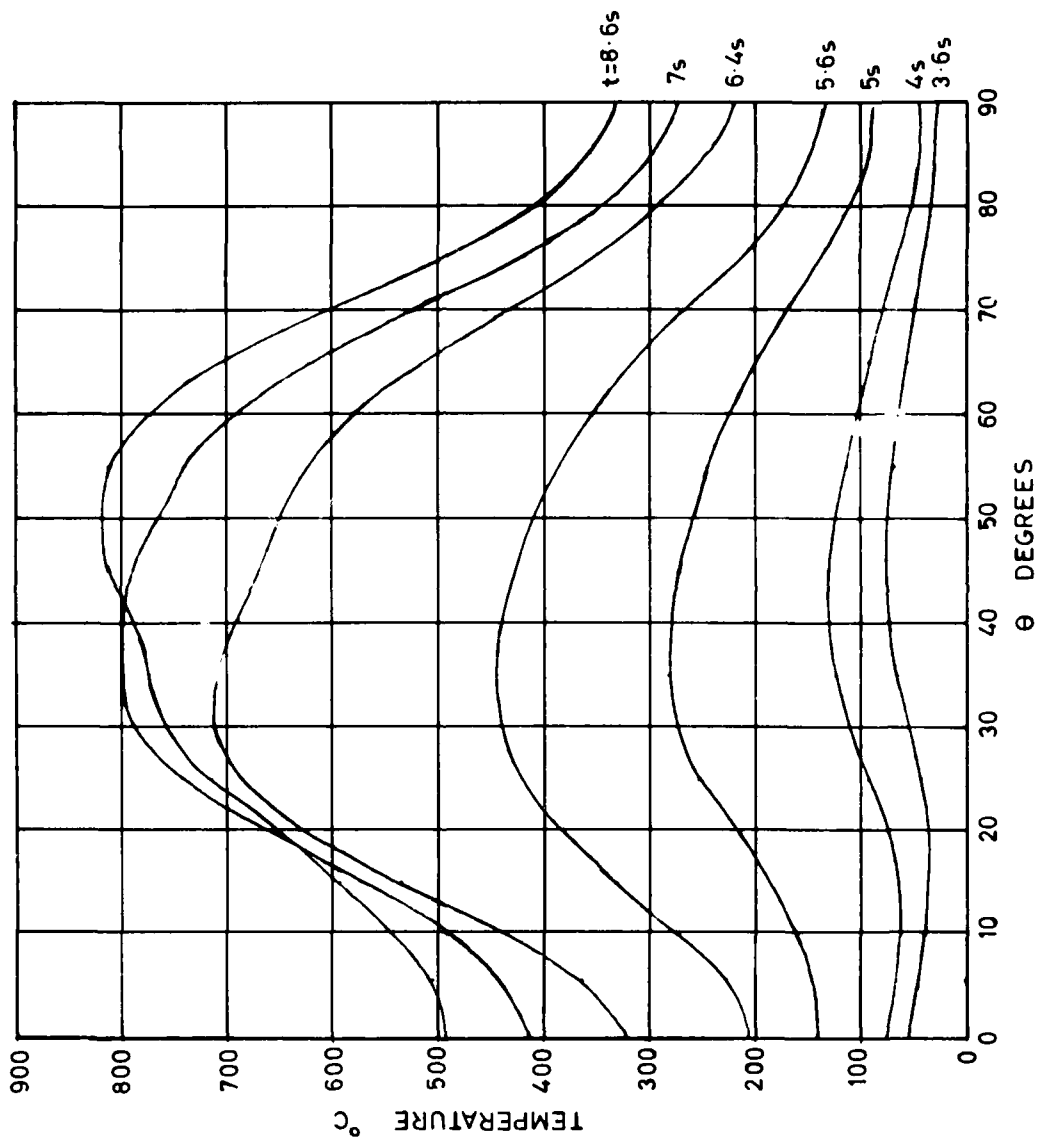


Figure 21. Derived outer surface temperature distribution ( $\phi=0$ )

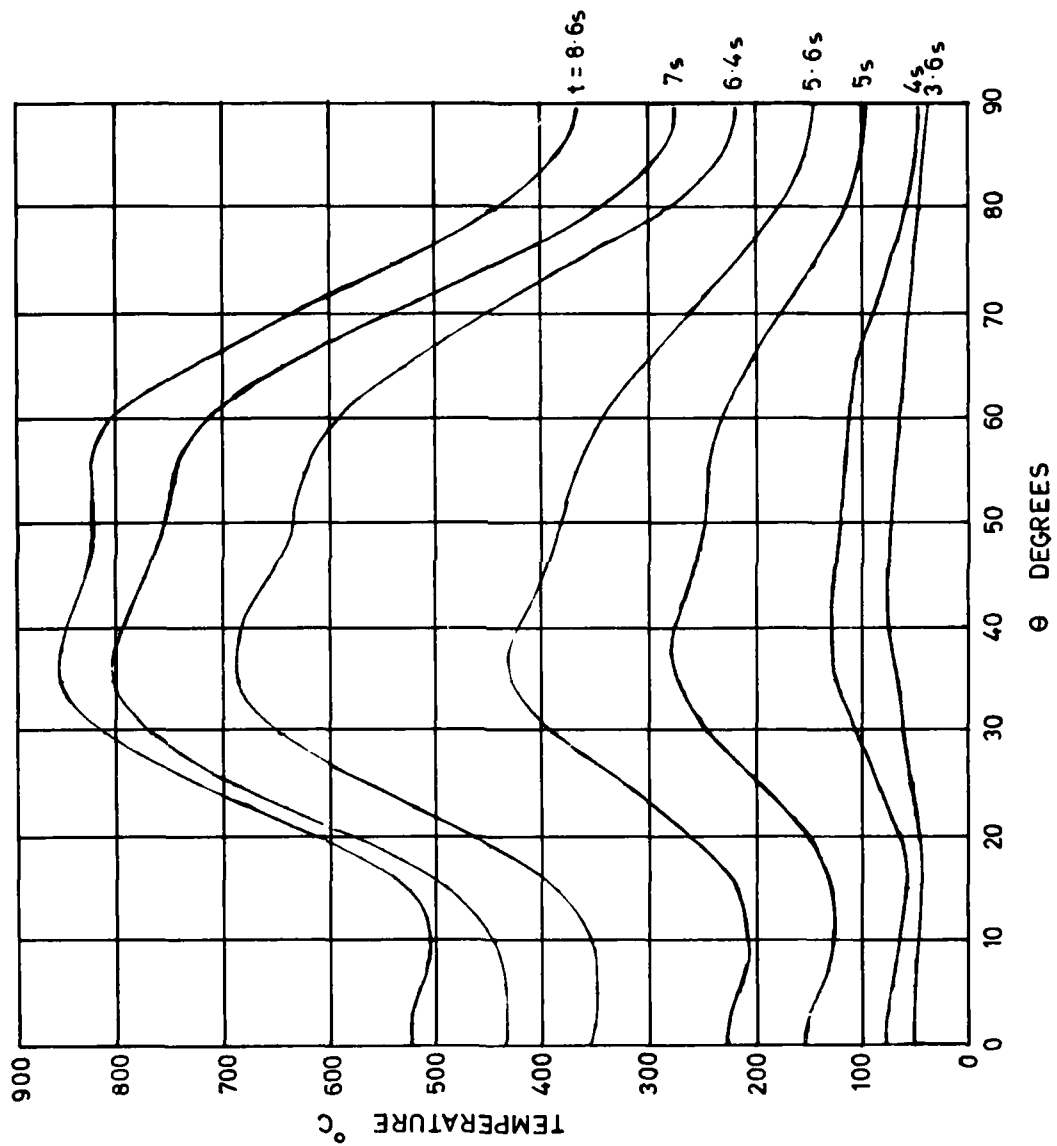


Figure 22. Derived outer surface temperature distribution ( $\phi=120^\circ$ )

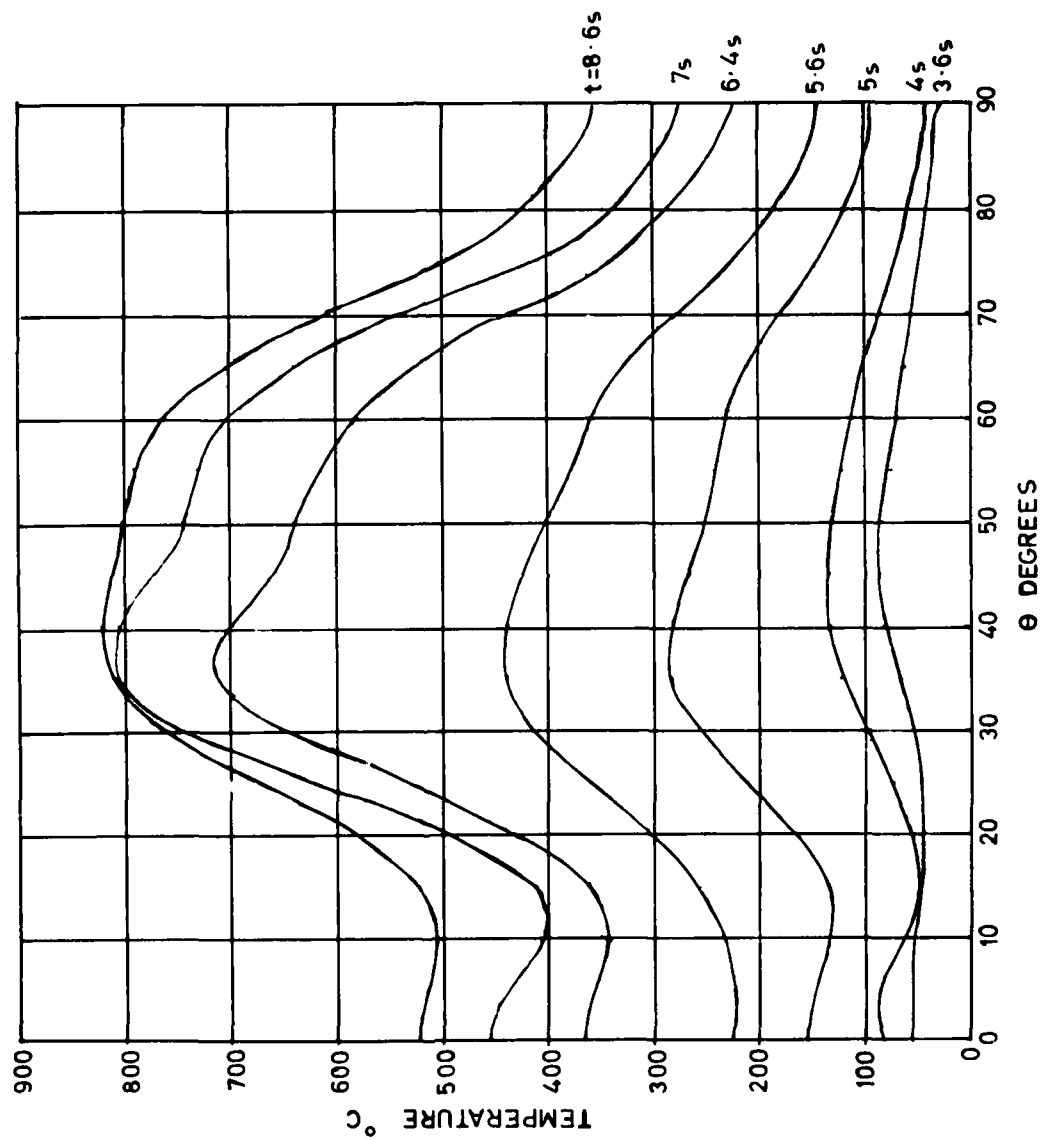


Figure 23. Derived outer surface temperature distribution ( $\theta = -120^\circ$ )

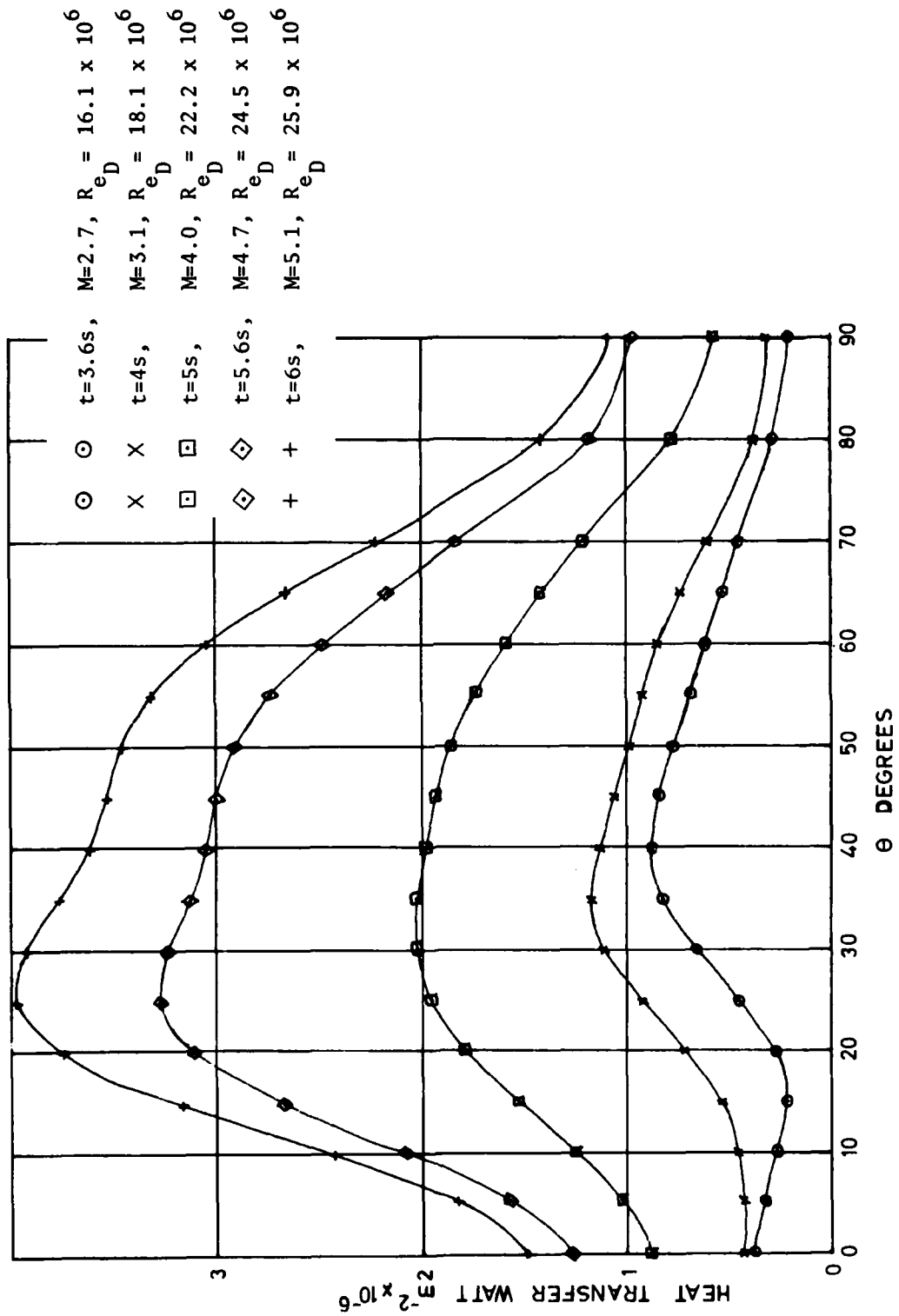


Figure 24. Derived outer surface heat transfer distribution ( $\phi=0$ ,  $t \leq 6s$ ).

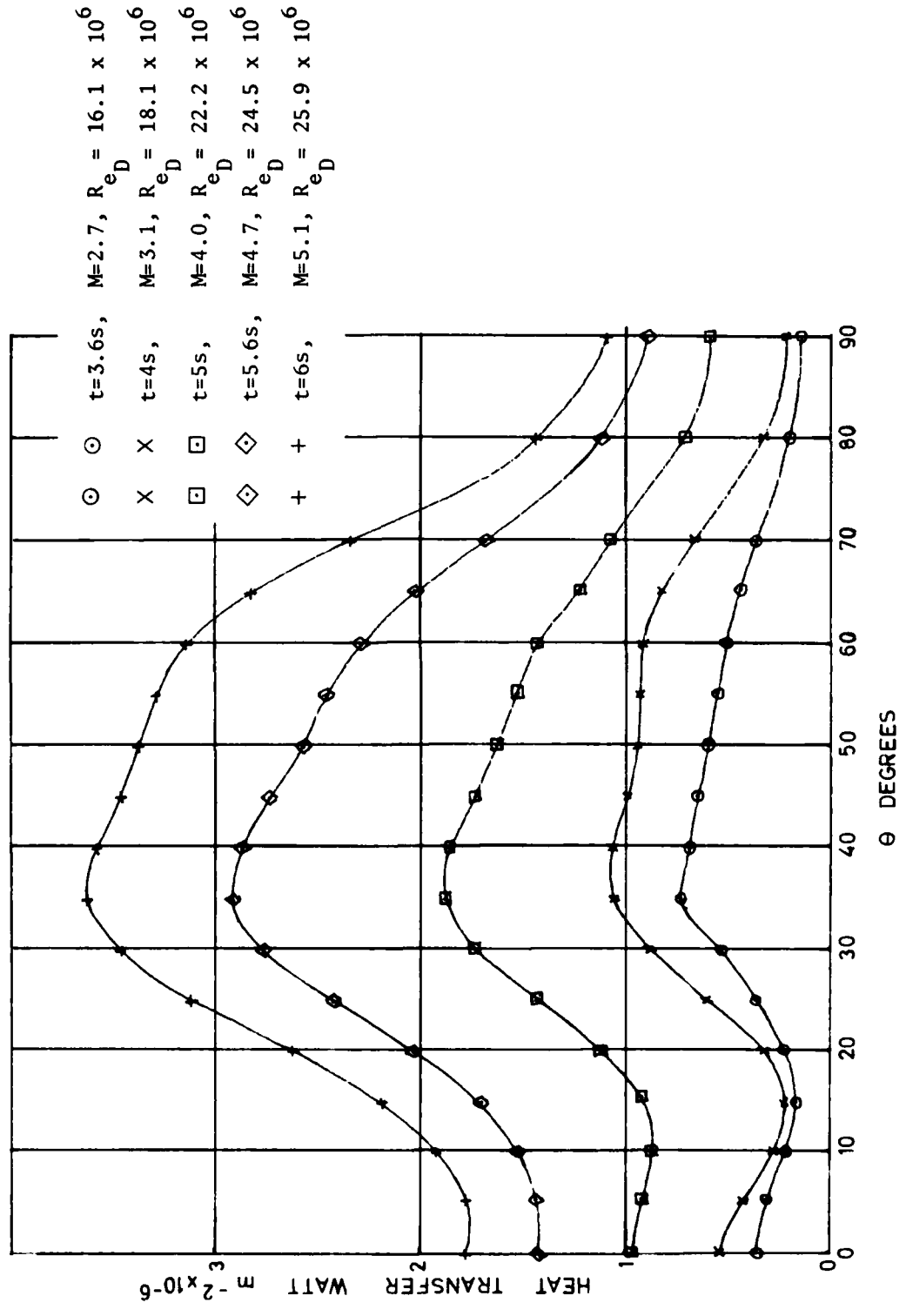


Figure 25. Derived outer surface heat transfer distribution ( $\phi=120^\circ$ ,  $t \leq 6s$ ).

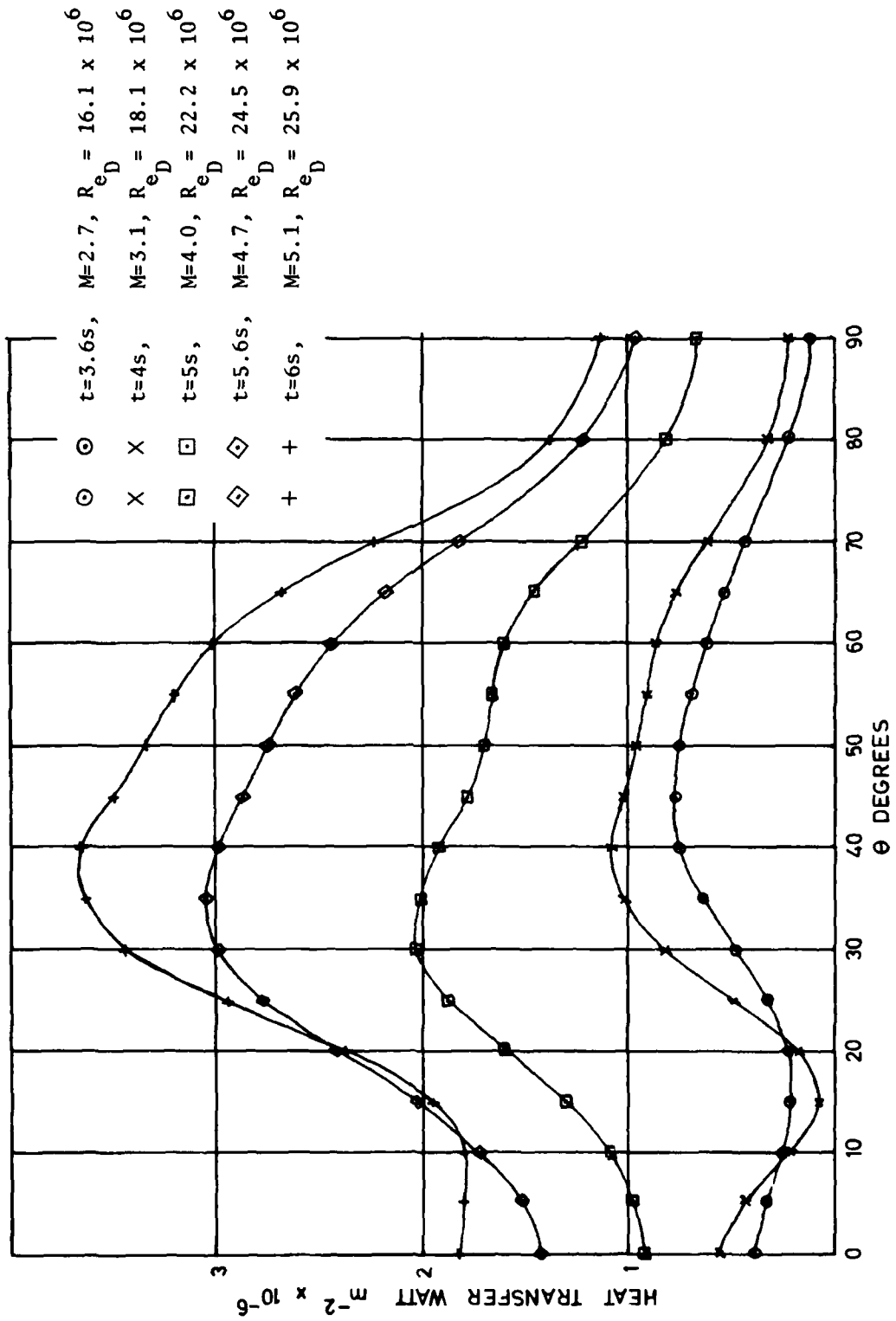


Figure 26. Derived outer surface heat transfer distribution ( $\phi = -120^\circ$ ,  $t \leq 6s$ ).

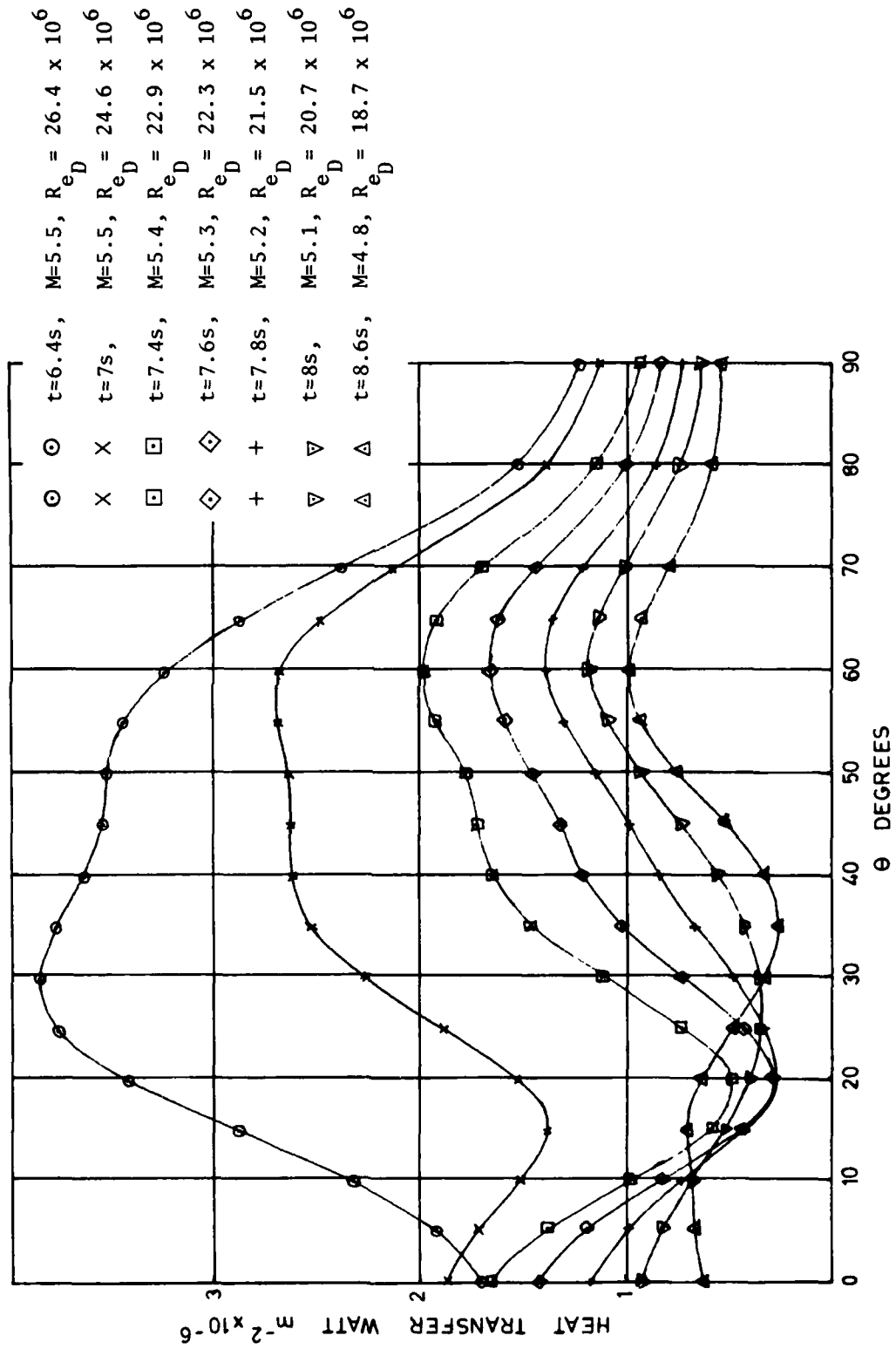


Figure 27. Derived outer surface heat transfer distribution ( $\phi=0$ ,  $t \geq 6.4s$ ).

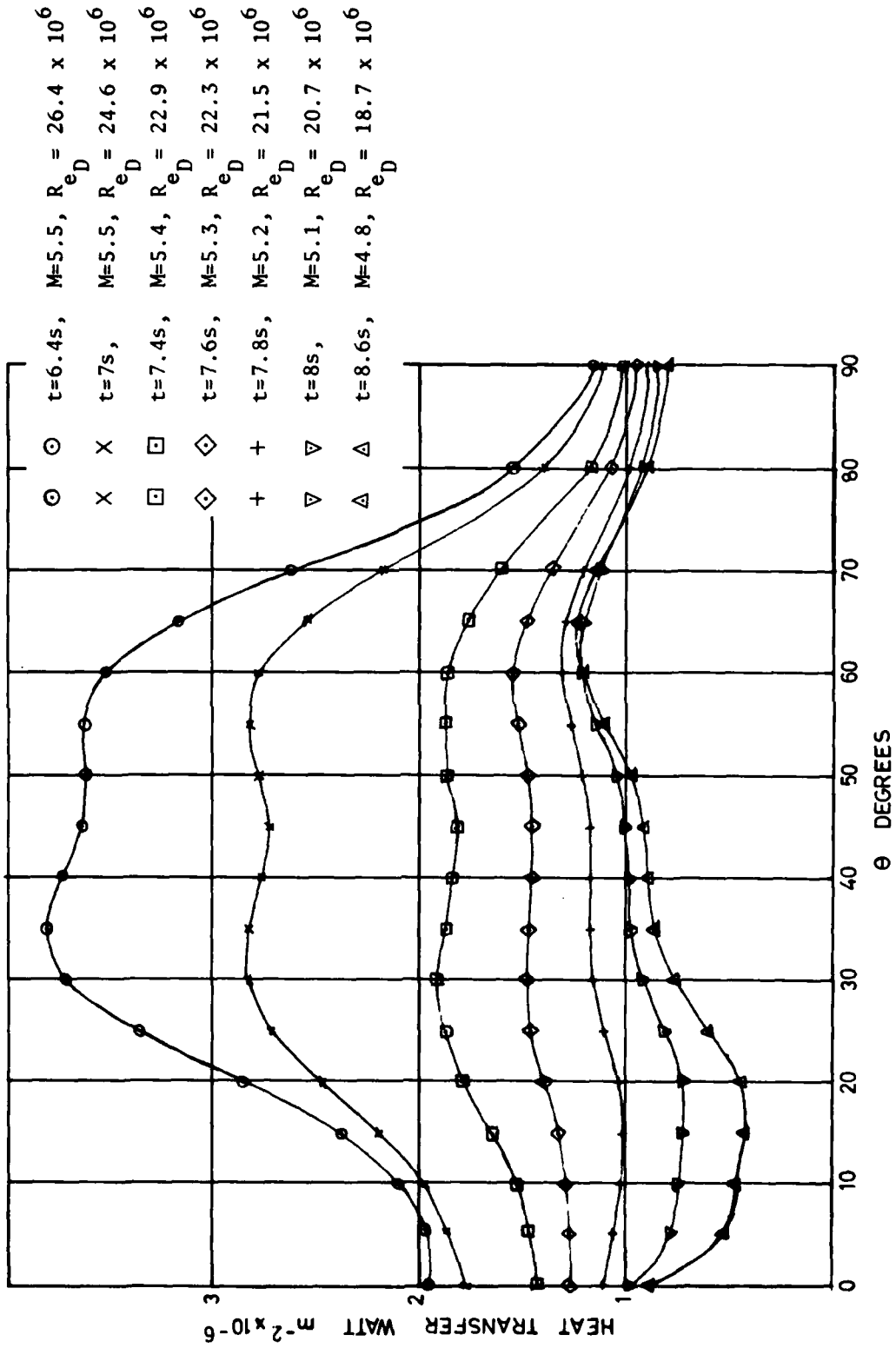


Figure 28. Derived outer surface heat transfer distribution ( $\phi=120^\circ$ ,  $t \geq 6.4s$ ).

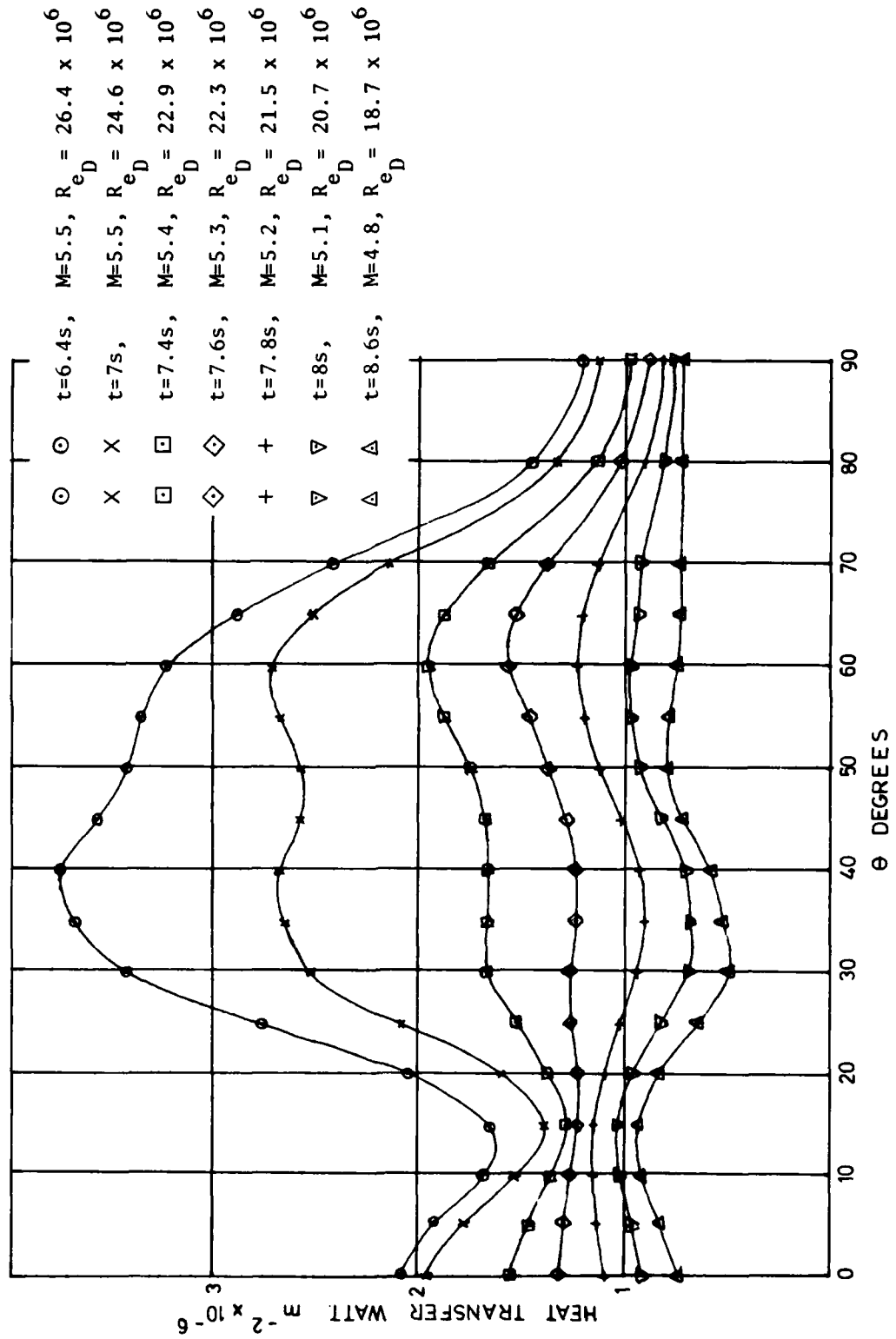


Figure 29. Derived outer surface heat transfer distribution ( $\phi = -120^\circ$ ,  $t \geq 6.4s$ ).

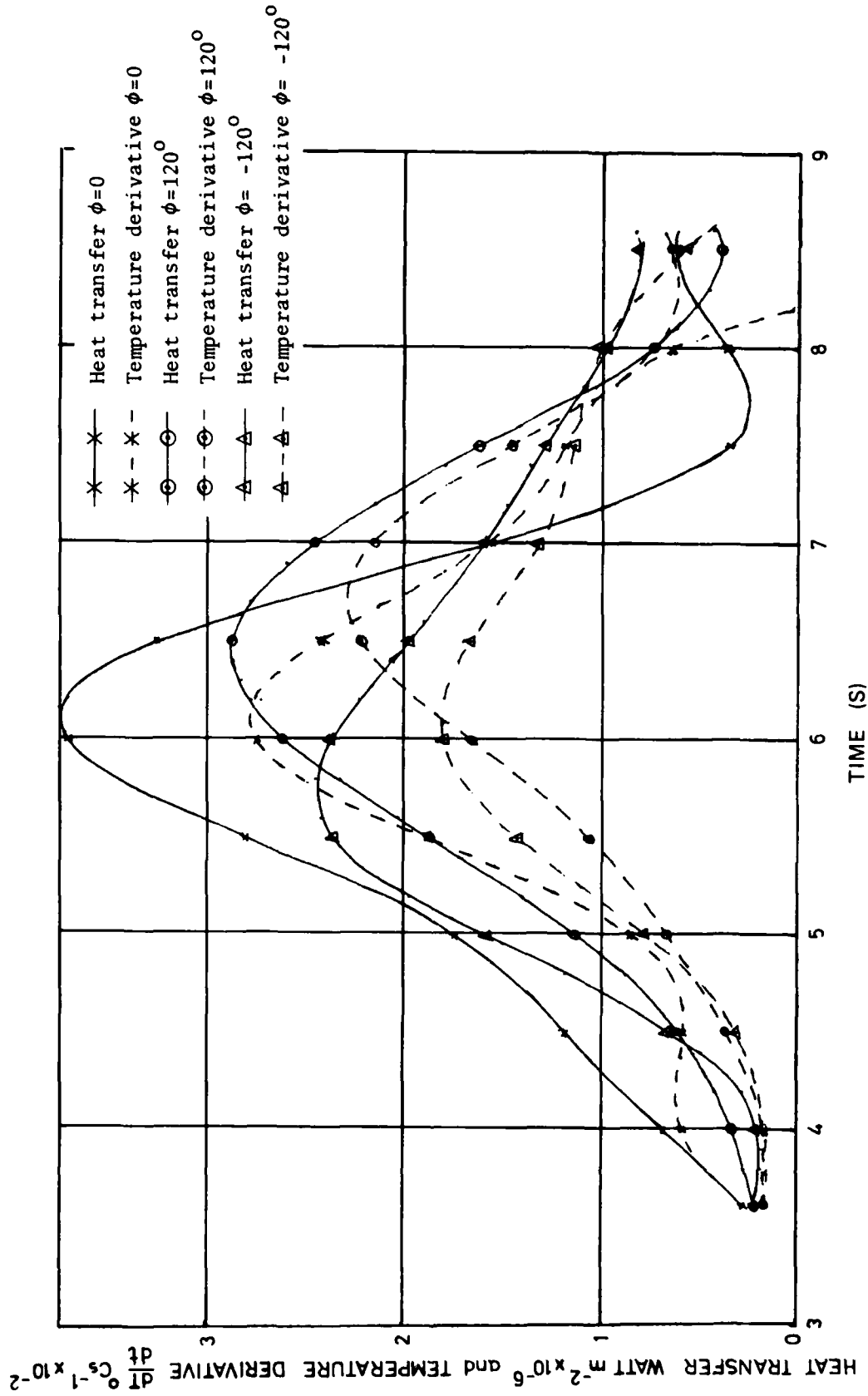


Figure 30. Outer surface heat transfer and inner surface temperature time derivative for  $\theta=20^\circ$ .

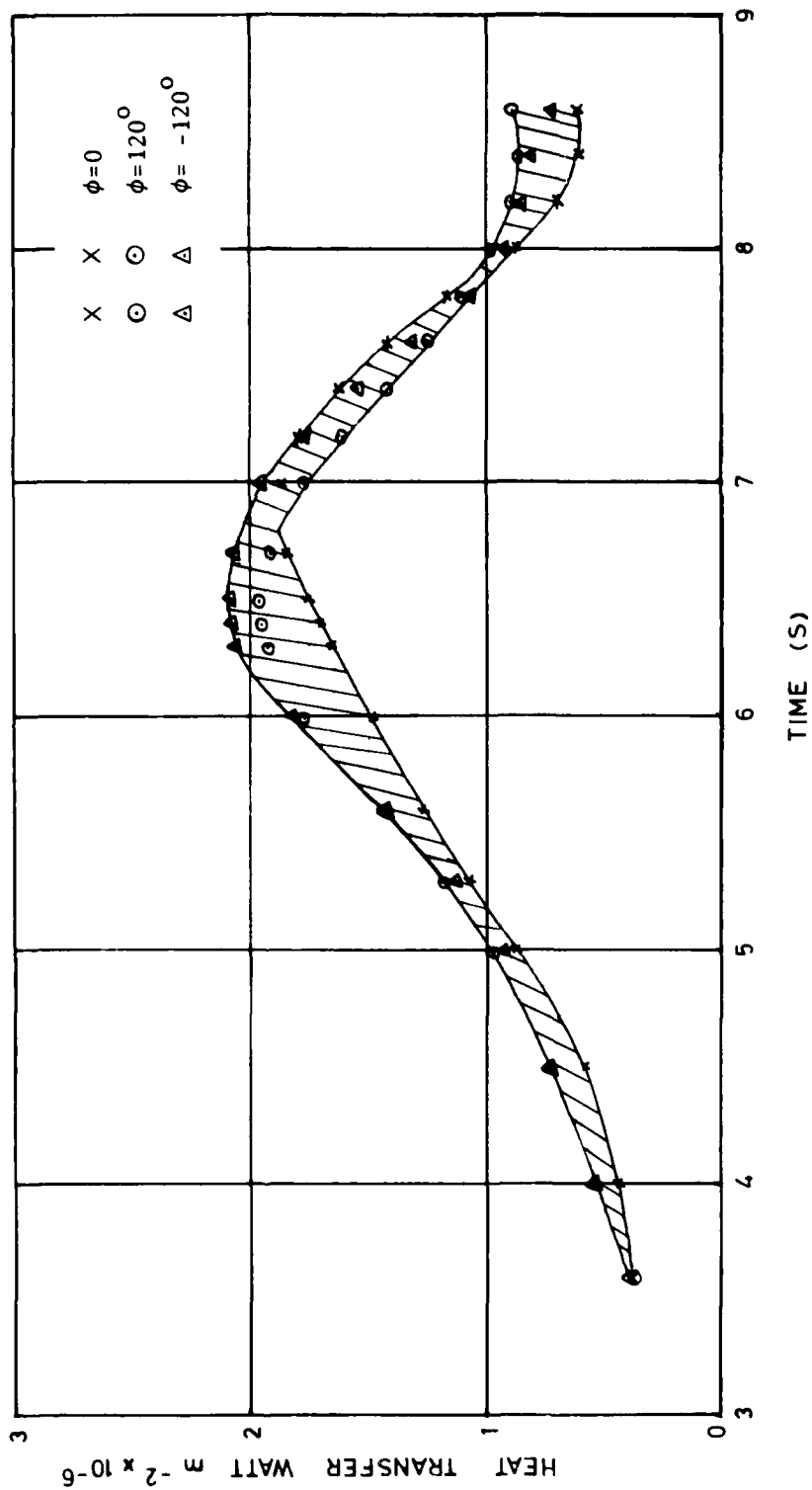


Figure 31. Scatter of derived outer surface heat transfer at stagnation point,  $\theta=0$

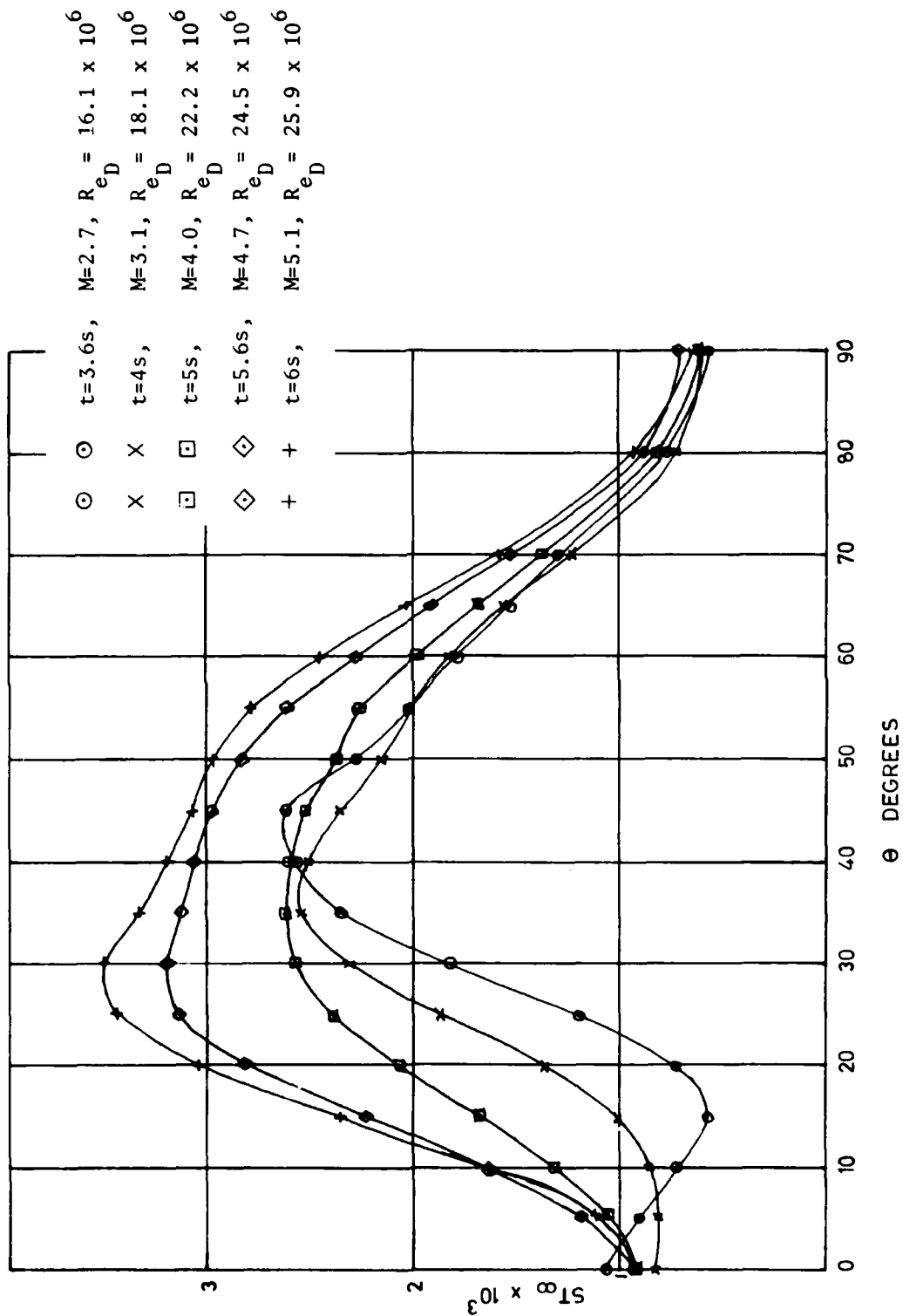


Figure 32. Stanton number distribution ( $\phi=0$ ,  $t \leq 6s$ ).

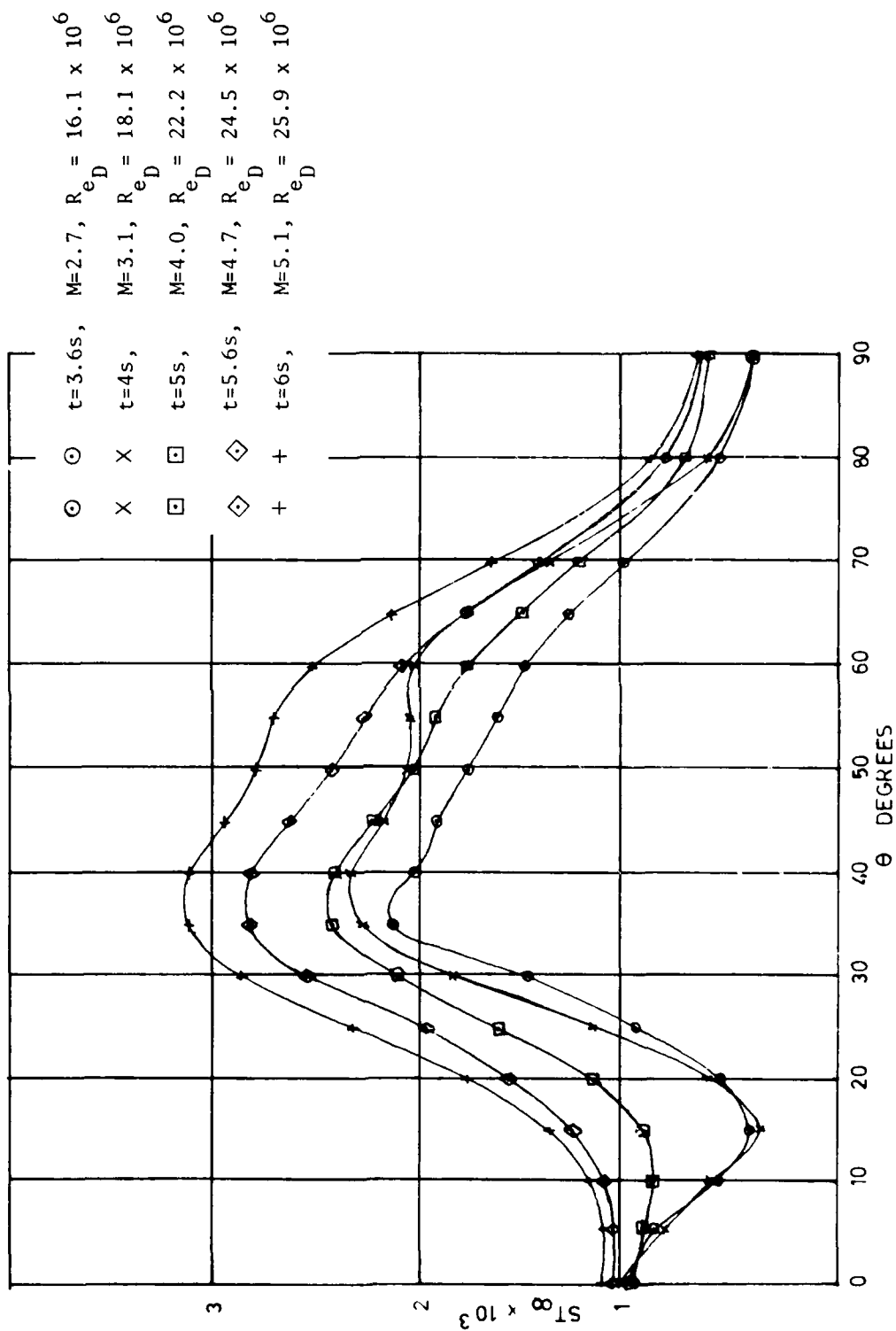


Figure 33. Stanton number distribution ( $\phi=120^\circ$ ,  $t \leq 6s$ ).

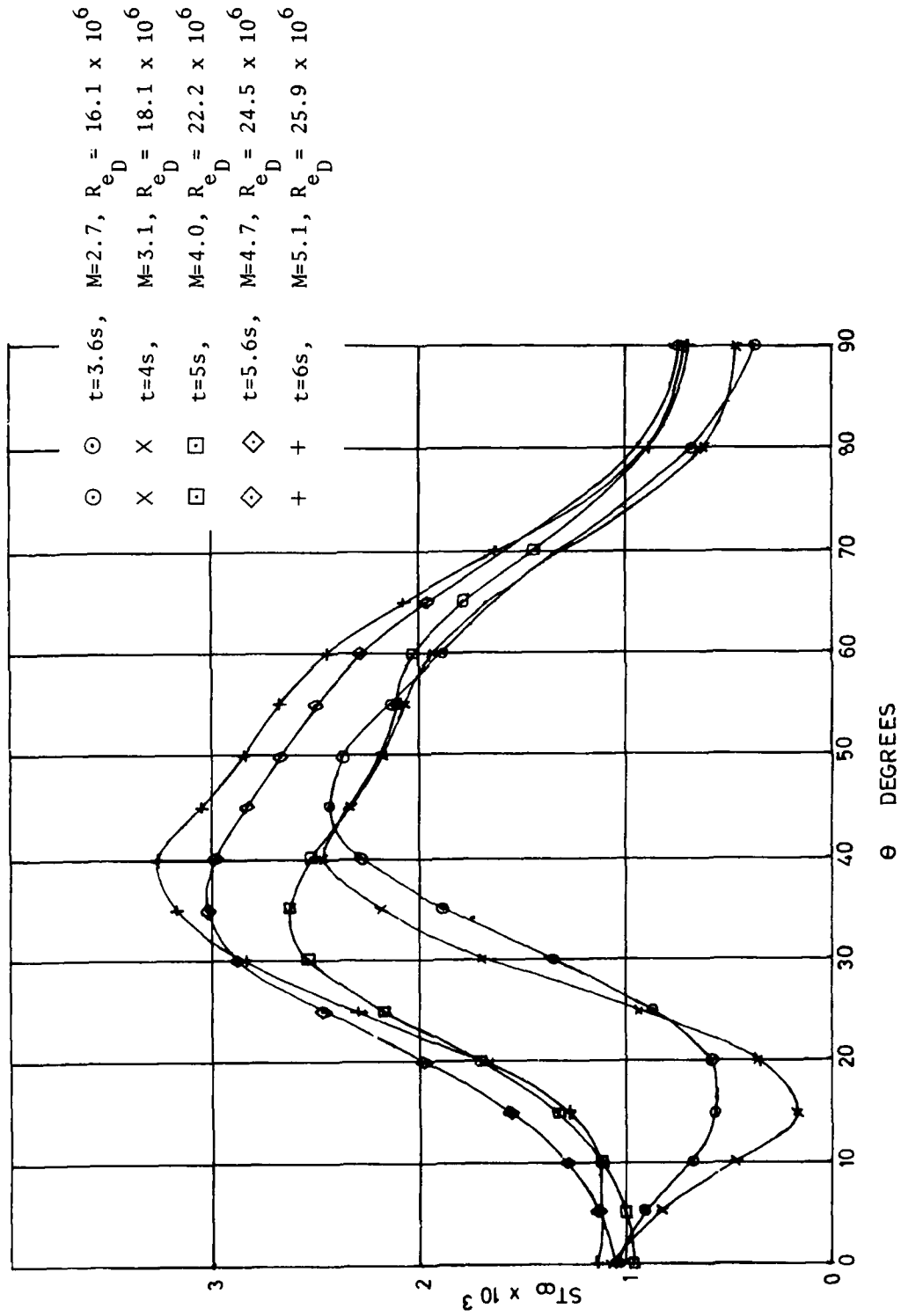


Figure 34. Stanton number distribution ( $\phi = -120^\circ$ ,  $t \leq 6s$ ).

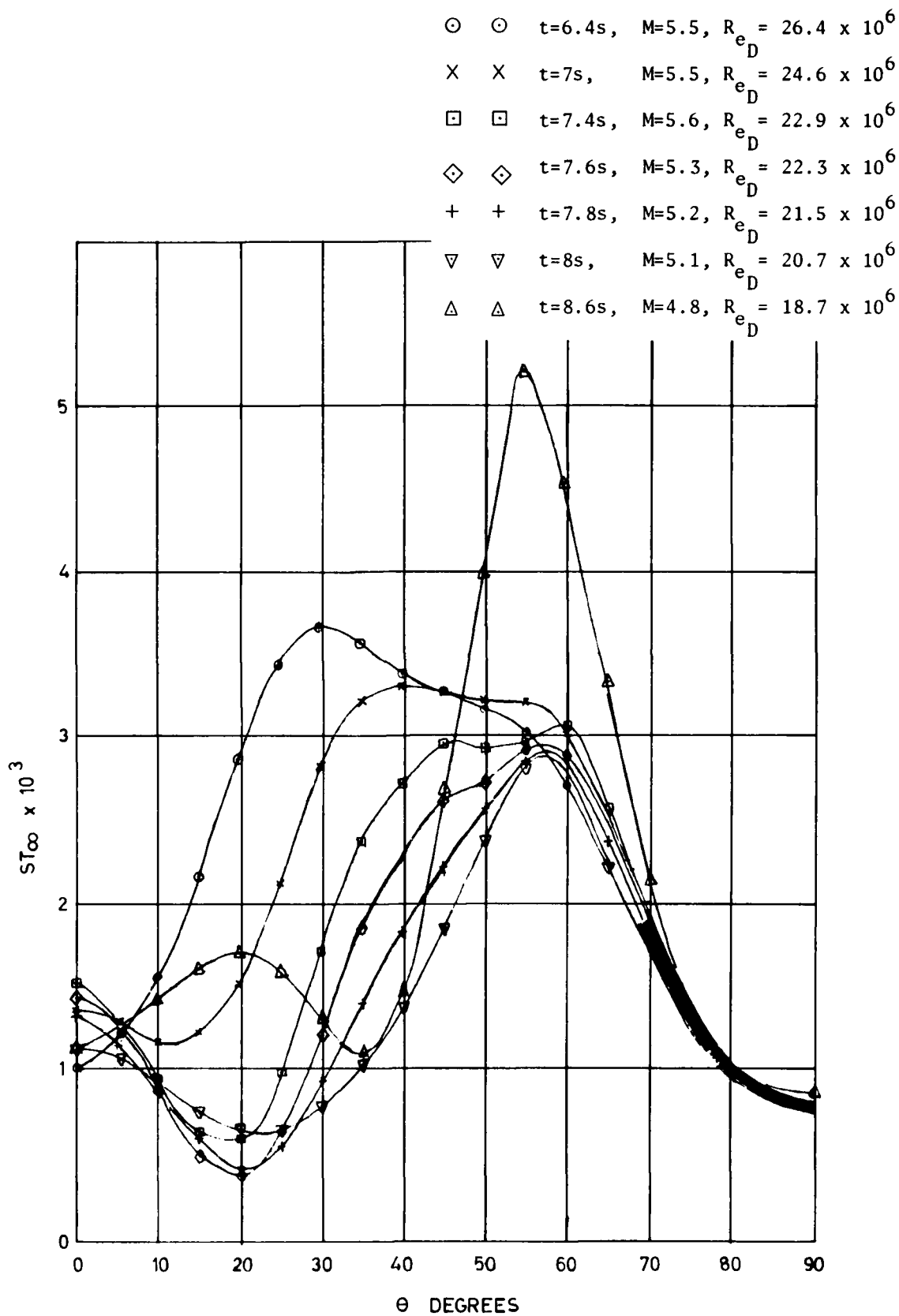


Figure 35. Stanton number distribution ( $\phi=0$ ,  $t \geq 6.4s$ ).

WSRL-0069-TR  
Figure 36

- |   |   |  |
|---|---|--|
| ⊙ | ⊙ | t=6.4s, M=5.5, $R_{eD} = 26.4 \times 10^6$ |
| × | × | t=7s, M=5.5, $R_{eD} = 24.6 \times 10^6$   |
| ⊠ | ⊠ | t=7.4s, M=5.4, $R_{eD} = 22.9 \times 10^6$ |
| ◇ | ◇ | t=7.6s, M=5.3, $R_{eD} = 22.3 \times 10^6$ |
| + | + | t=7.8s, M=5.2, $R_{eD} = 21.5 \times 10^6$ |
| ▽ | ▽ | t=8s, M=5.1, $R_{eD} = 20.7 \times 10^6$   |

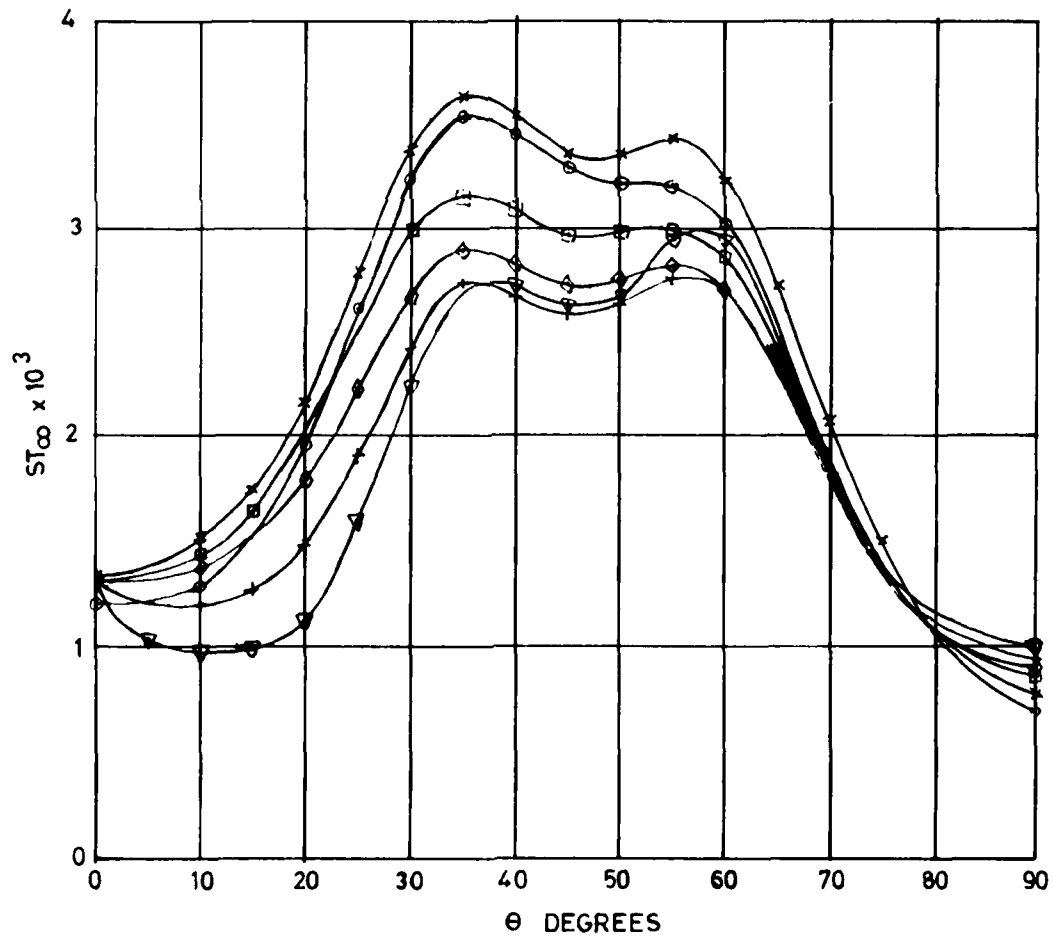


Figure 36. Stanton number distribution ( $\phi=120^\circ$ ,  $t \geq 6.4s$ ).

⊙	⊙	t=6.4s, M=5.5, $R_{eD} = 26.4 \times 10^6$
×	×	t=7s, M=5.5, $R_{eD} = 24.6 \times 10^6$
□	□	t=7.4s, M=5.4, $R_{eD} = 22.9 \times 10^6$
◇	◇	t=7.6s, M=5.3, $R_{eD} = 22.3 \times 10^6$
+	+	t=7.8s, M=5.2, $R_{eD} = 21.5 \times 10^6$
▽	▽	t=8s, M=5.1, $R_{eD} = 20.7 \times 10^6$
△	△	t=8.6s, M=4.8, $R_{eD} = 18.7 \times 10^6$

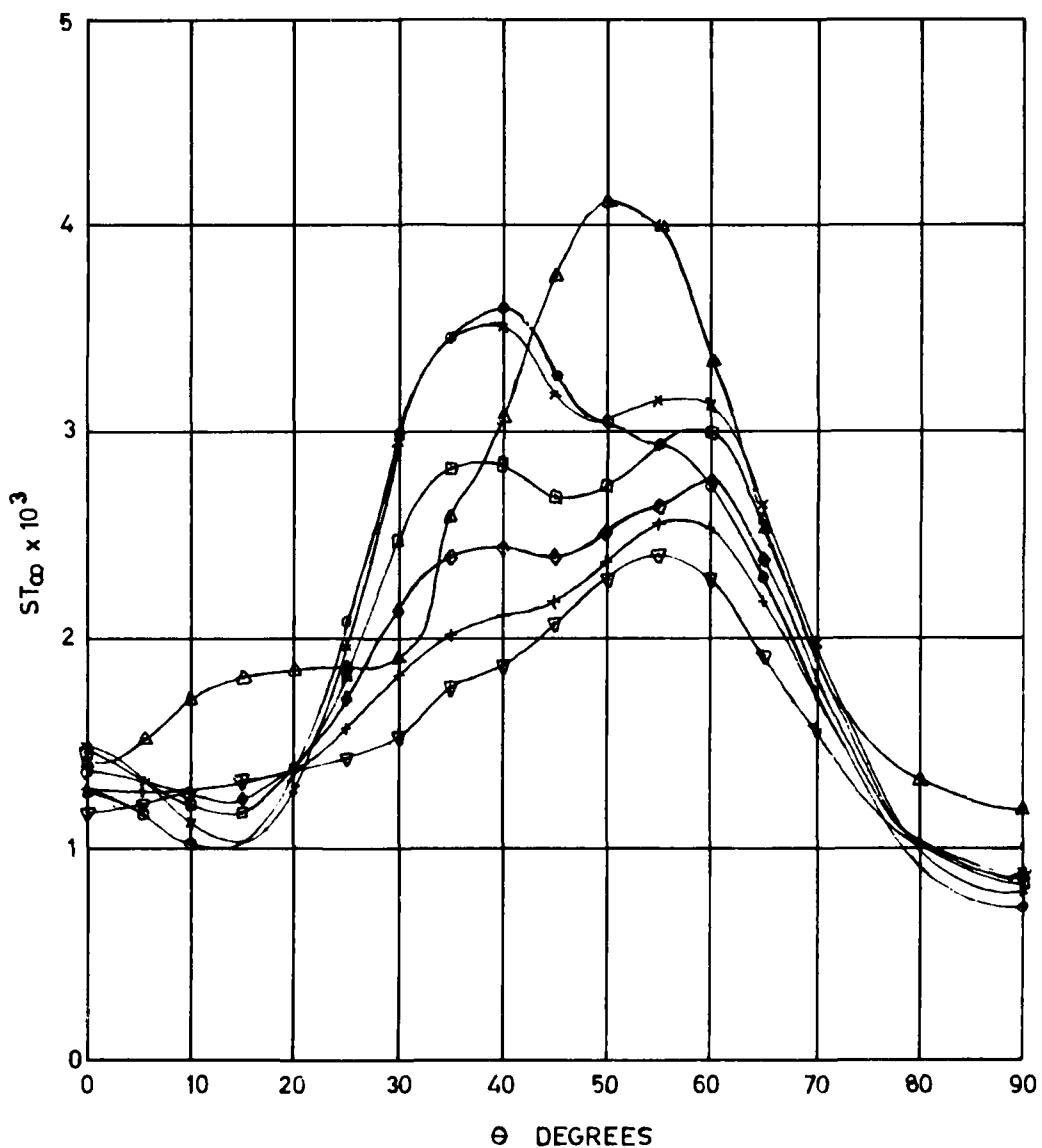


Figure 37. Stanton number distribution ( $\phi = -120^\circ$ ,  $t \geq 6.4s$ ).

X X  $\phi=0$   
O O  $\phi=120^\circ$   
 $\Delta$   $\Delta$   $\phi=-120^\circ$

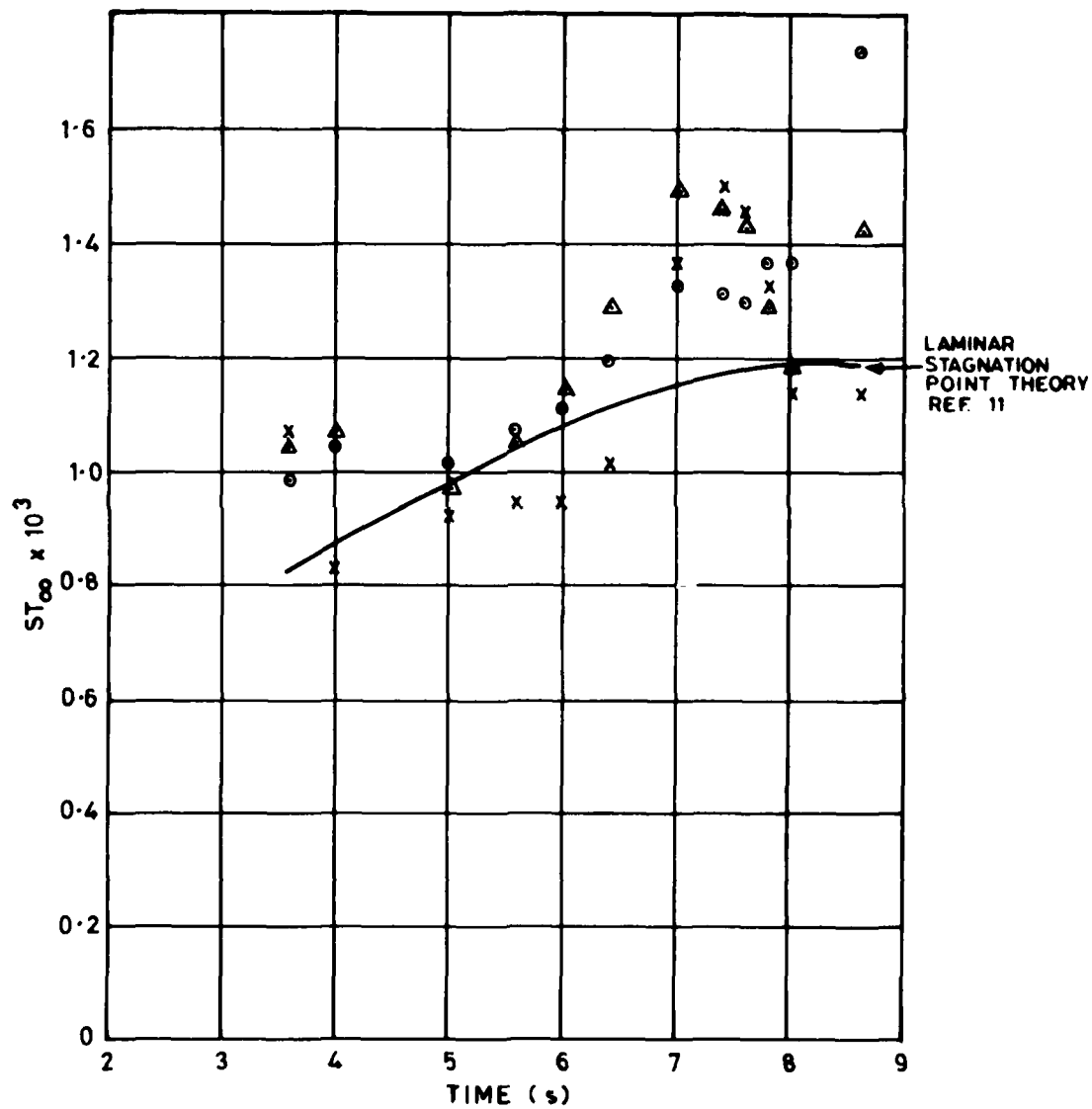


Figure 38. Comparison of derived stagnation point Stanton number with laminar theory.

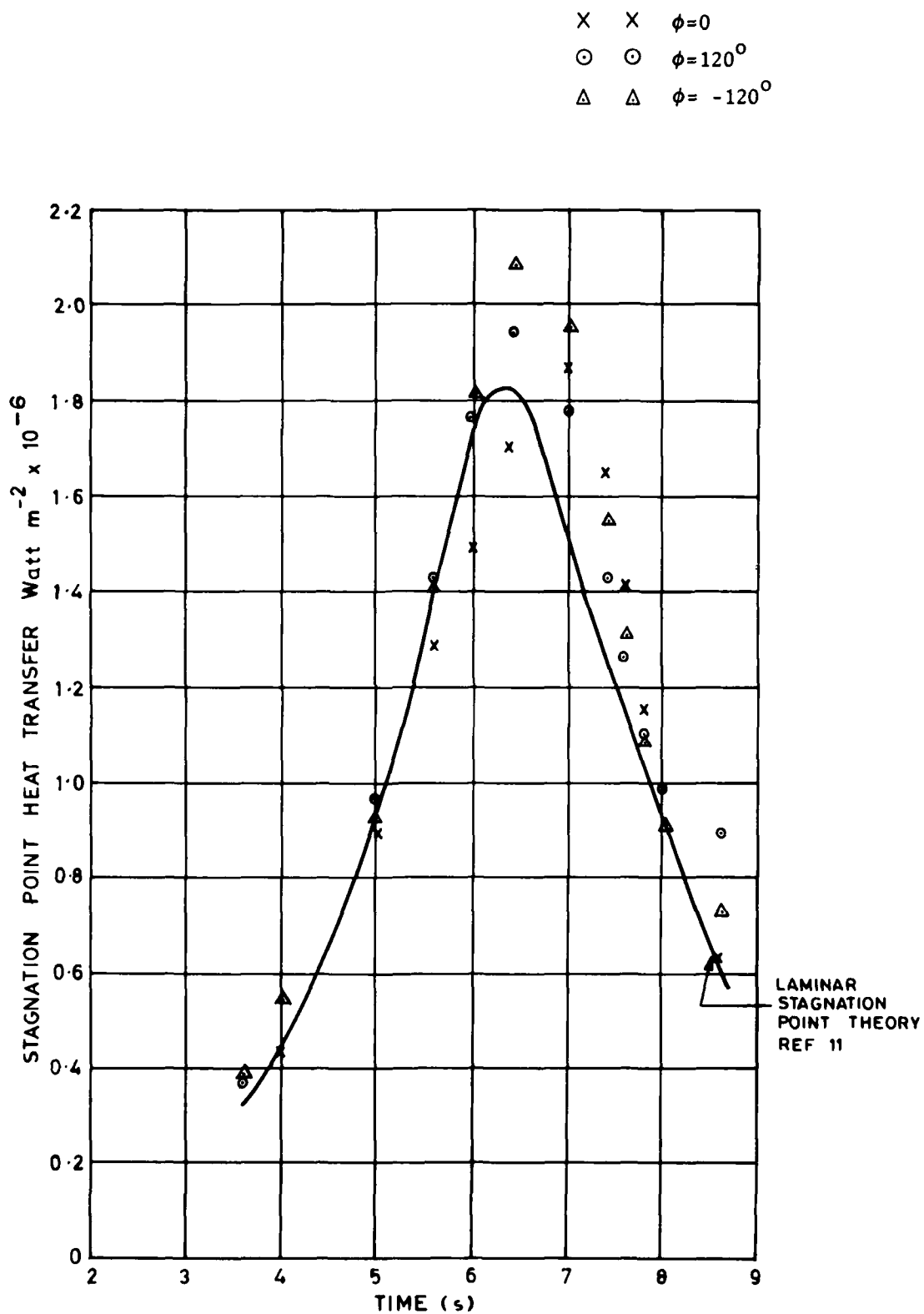


Figure 39. Comparison of derived stagnation point heat transfer with laminar theory.

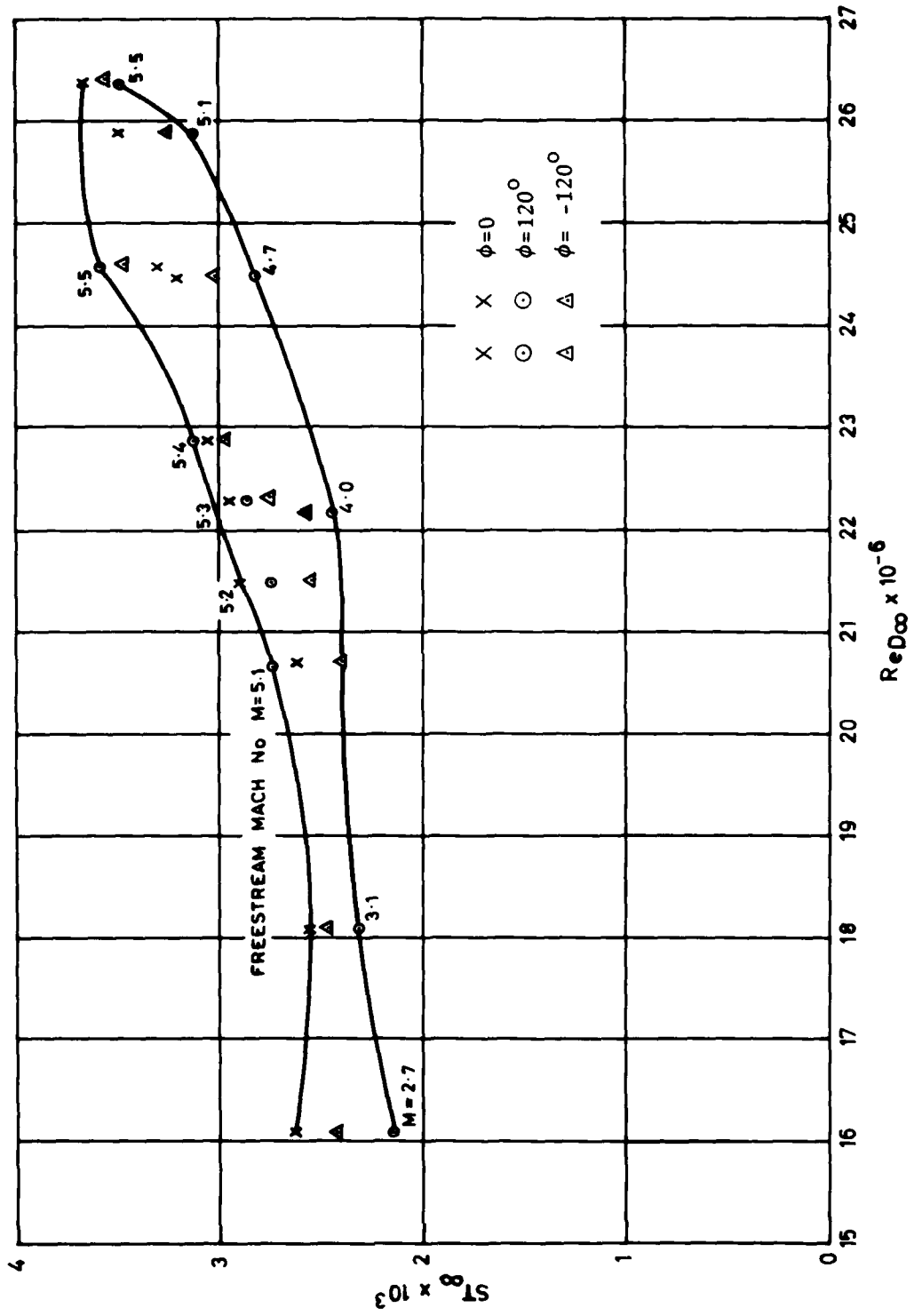


Figure 40. Peak turbulent heating envelope.

## DISTRIBUTION

Copy No.

## EXTERNAL

## In United Kingdom

Defence Scientific and Technical Representative, London	1
RAE, Aero Department	2 - 3
RAE, Space Department	4
RAE, Weapons Department	5 - 6
RAE, Weapons Department, Attention Mr R.L. Dommett	7 - 8
RAE, Bedford	9
RAE, Library	10
RARDE	11
TTCP, UK National Leader Panel W-2	12 - 15
Aeronautical Research Council	16 - 17
Aircraft Research Association (Bedford)	18
CAARC Secretary	19
National Lending Library of Science and Technology	20
Royal Aeronautical Society, Library	21

## In United States of America

Counsellor, Defence Science, Washington	22
Defence Research and Development Attache, Washington	23
Applied Physics Laboratory, Johns Hopkins University	24
Air Force Armament Testing Laboratory	25
Ballistics Research Laboratories	26
Edgewood Arsenal	27
Eglin Air Force Base	28
NASA	29 - 32
Naval Surface Weapons Center	
Dahlgren	33
White Oak	34
Naval Weapons Center	35
Naval Ship Research and Development Center	36
Picatinny Arsenal	37
Redstone Arsenal	38
TTCP US National Leader Panel W-2	39 - 42
Wright-Patterson Air Force Base, Library	43
American Institute of Aeronautics and Astronautics, Library	44
Pacific Technical Information Services, Northrop Institute of Technology	45

	Copy No.
Applied Mechanics Reviews	46
Arnold Engineering Development Center	47
ARO Inc.	48
Sandia Corporation, Library	49
In Canada	
Defence Research Establishment, Valcartier	50
NAE, Ottawa	51
TTCP, Canadian National Leader Panel W-2	52 - 55
University of Toronto, Institute of Aerospace Studies	56
In Europe	
AGARD, Brussels	57 - 62
In India	
Aeronautical Development Establishment, Bangalore	63
Indian Institute of Science, Bangalore (Dept of Aero Engineering)	64
Indian Institute of Technology, Madras (Dept of Aero Engineering)	65
Hindustan Aeronautics Ltd, Bangalore	66
National Aeronautical Lab, Bangalore	67 - 68
Space Science and Technology Centre, Trivandrum	69
In Australia	
Chief Defence Scientist	70
Deputy Chief Defence Scientist	71
Superintendent, Science and Technology Programmes	72
Controller, Projects and Analytical Studies	73
Air Force Scientific Adviser	74 - 75
Army Scientific Adviser	76 - 77
Navy Scientific Adviser	78 - 79
Central Studies Establishment	80
Director, Joint Intelligence Organisation (DDSTI)	81
Defence Information Services Branch (for microfilming)	82
Defence Information Services Branch for:	
United Kingdom, Ministry of Defence, Defence Research Information Centre (DRIC)	83
United States, Department of Defense, Defense Documentation Center	84 - 95
Canada, Department of National Defence, Defence Science Information Service	96
New Zealand, Ministry of Defence	97
Australian National Library	98
Defence Library, Campbell Park	99

	Copy No.
BDRSS, Canberra	100
Department of Defence, Melbourne	
Chief Superintendent, Aeronautical Research Laboratories	101
Superintendent, Aerodynamics Division, Aeronautical Research Laboratories	102
DA Secomb, for data exchange agreement, Aeronautical Research Laboratories	103
Superintendent, Mechanical Engineering Division, Aeronautical Research Laboratories	104
Library, Aeronautical Research Laboratories	105
Library, Materials Research Laboratories	106
Department of Defence, Adelaide	
Aircraft Research and Development Unit, Edinburgh	107
Department of Productivity, Melbourne	
Government Aircraft Factories	108
RAAF Academy, Point Cook	109
Commonwealth Aircraft Corporation	110
Institution of Engineers, Australia	111
 WITHIN DRCS	
Chief Superintendent, Weapons Systems Research Laboratory	112
Superintendent, Aeroballistics Division	113
Senior Principal Research Scientist, Ballistics	114
Principal Officer, Dynamics Group	115
Principal Officer, Aerodynamics Research Group	116
Principal Officer, Ballistic Studies Group	117
Principal Officer, Field Experiments Group	118
Principal Officer, Flight Research Group	119
Author	120
DRCS Library	121 - 122
AD Library	123 - 128
Spares	129 - 145

D  
FI  
g.